Costimulatory molecule-related gene-based prognostic signature and immune characteristics in osteosarcoma

Sen Cai, Lingtao Xu, Shaole Wan, Yonghui Shen*, Zengyong Hu*

Hand Surgery/Wound Reconstruction Surgery, Lishui Hospital of Wenzhou Medical University, The First Affiliated Hospital of Lishui University, Lishui People's Hospital, Lishui, Zhejiang, China

Submitted: 8 January 2026; **Accepted:** 15 February 2026
Online publication: 1 May 2026

Arch Med Sci 2026; 22 (5): 2968–2994
DOI: https://doi.org/10.5114/aoms/218150
Copyright © 2026 Termedia & Banach

***Corresponding authors:**
Zengyong Hu
Yonghui Shen
Hand Surgery/Wound Reconstruction Surgery
Lishui Hospital of Wenzhou Medical University
The First Affiliated Hospital of Lishui University
Lishui People's Hospital
Lishui, Zhejiang, China
E-mail: huzengyong007@163.com, shenyonghui1022@163.com

Abstract

Introduction: Osteosarcoma (OSA) is a primary malignant bone tumor with a poor prognosis. Costimulatory molecule-related genes (CMRGs) are crucial for T cell-mediated antitumor immunity, yet their prognostic and therapeutic value in OSA remains unclear.

Material and methods: Non-negative matrix factorization (NMF) clustering was used to define CMRG-based subtypes. Prognostic signature genes were selected using univariate Cox, LASSO, and multivariate regression analyses. The predictive performance of the model was assessed using ROC curves, calibration plots, and decision curve analysis (DCA). Immune infiltration and immune checkpoint differences were evaluated via ssGSEA. Drug sensitivity was predicted using CellMiner, and gene expression was validated by qRT-PCR in OSA cells.

Results: This study identified five characteristic genes related to the prognosis of OSA and constructed a prognostic model. The evaluation results indicated that the model has favorable predictive performance, with calibration curves and DCA indicating good agreement between predicted and observed survival probabilities. Furthermore, immunotherapy response analysis revealed that patients with lower risk scores had more favorable immune responses and lower rates of disease metastasis. Notably, DMAPT, Obatoclax, 8-Chloro-adenosine, and Palbociclib showed a significant positive correlation with MYC. Additionally, qRT-PCR results indicated that EPYC, SCD1, and AOC3 were significantly overexpressed in OSA cells.

Conclusions: This study integrates CMRG-based subtyping, risk modeling, immune profiling, and experimental validation in OSA. The identified biomarkers may help inform personalized treatment and survival risk stratification in OSA patients.

Key words: osteosarcoma, costimulatory molecule, prognostic gene signature, immunological characteristics.

Introduction

Osteosarcoma (OSA) is a highly aggressive primary malignant bone tumor originating from mesenchymal cells, predominantly affecting children and adolescents [1]. It is characterized by a high propensity for early metastasis, particularly to the lungs, contributing to poor prognosis [2, 3]. While localized OSA has a 5-year survival rate of ~60%, this rate drops to ~20% in metastatic cases [4, 5]. Despite surgical and chemotherapeutic advances, overall survival has not significantly improved over the past two decades [6], largely due to tumor heterogeneity, genetic alterations, and chemoresistance [7–9].

Creative Commons licenses: This is an Open Access article distributed under the terms of the Creative Commons Attribution-NonCommercial-ShareAlike 4.0 International (CC BY -NC -SA 4.0). License (http://creativecommons.org/licenses/by-nc-sa/4.0/).

Recent studies have highlighted that non-coding RNAs and epigenetic modifications are important contributors to OSA chemoresistance. For instance, METTL3-mediated m6A methylation stabilizes LINC00520, which enhances glycolysis and cisplatin resistance by stabilizing ENO1 protein [10]. In addition, ferroptosis has emerged as a key mechanism in OSA progression and therapy response. Exosome-mediated delivery of miR-144-3p was shown to inhibit OSA cell proliferation and invasion by promoting ferroptosis through ZEB1 suppression [11].

Moreover, dysregulated cell death pathways such as autophagy and ferroptosis may be therapeutically exploitable. Overexpression of apolipoprotein E (APOE) has been reported to suppress OSA growth by inducing both autophagy and ferroptosis via inhibition of the mTOR/Stat3 signaling pathway [12]. These findings underscore the need for better prognostic markers and novel therapeutic strategies in OSA.

The tumor microenvironment (TME) – comprising tumor cells, immune cells, stromal components, and cytokines – plays a critical role in cancer progression, metastasis, and immunotherapy efficacy [13]. In this context, costimulatory molecules are essential in mediating T cell activation and immune modulation [8, 14, 15]. These molecules, primarily members of the B7-CD28 and TNF superfamilies, are involved in delivering the second signal required for effective T cell responses [16–21]. While studies have implicated B7 family members such as PD-L1 and B7-H1 in OSA immune regulation [18], a comprehensive understanding of costimulatory molecule-related genes (CMRGs) in OSA remains lacking.

To address this, we conducted a systematic analysis of CMRG expression patterns, identified molecular subtypes, and developed a prognostic model using characteristic CMRGs. We further evaluated immune infiltration, predicted drug sensitivity, and validated key genes via qRT-PCR. This integrative approach aims to elucidate the immunological and prognostic significance of CMRGs in OSA and to support the development of individualized treatment strategies.

Material and methods

Data origin

mRNA expression data related to TARGET-OS were retrieved from the TCGA database (https://portal.gdc.cancer.gov/). Patient clinical information was sourced from the TARGET database (https://ocg.cancer.gov/programs/target). Additionally, microarray datasets were obtained from the Gene Expression Omnibus (GEO) database (GSE21257 and GSE99671), while single-cell data came from GSE152048. To identify 60 CMRGs, we reviewed existing literature (Supplementary Table SI) [22]. The IMvigor210CoreBiologies package was employed to gather data on immunotherapy cohorts and relevant clinical details for bladder cancer (BLCA) patients undergoing immune checkpoint therapy.

Differential analysis and molecular subtype construction based on CMRGs

Using the "edgeR" package, differential analysis was performed on the GSE99671 dataset, comparing the normal group (N = 18) and the tumor group (OSA, N = 18) with criteria of |log fold change (FC)| > 0.585 and $p < 0.05$. The differentially expressed genes (OSA-DEGs) were intersected with CMRGs, resulting in CMRG-related differentially expressed genes (DECMRGs, Supplementary Table SII). The expression levels of the DECMRGs in both the normal and tumor groups were quantified, and a heatmap was generated. Based on the DECMRGs, the non-negative matrix factorization (NMF) clustering method was employed to classify the TARGET-OS dataset. Survival analysis of the three subtypes was conducted using Kaplan-Meier (KM) curves.

Immune status analysis of molecular subtypes

Using the "GSVA" package, single-sample gene set enrichment analysis (ssGSEA) was conducted to investigate the differences in immune-related functions and immune cell infiltration among the three subtypes. The ESTIMATE algorithm was employed to evaluate the stromal score, immune score, ESTIMATE score and tumor purity for each sample across the three subtypes. Clusters 2 and 3 were merged to form a new subtype. Subsequently, the "clusterProfiler" package was used to perform Gene Ontology (GO) and Kyoto Encyclopedia of Genes and Genomes (KEGG) enrichment analysis on the differentially expressed genes (group-DEGs) between Cluster 1 and the merged subtype (Supplementary Table SIII).

Selection of prognostic feature genes for OSA and construction of a prognostic model

Clinical data were merged with the expression levels of differentially expressed genes. The intersection of group-DEGs (|logFC| > 1, $p < 0.01$) and OSA-DEGs (|logFC| > 0.585, $p < 0.05$) was used as candidate genes. To reduce the risk of model overfitting, least absolute shrinkage and selection operator (LASSO) regression analysis was performed on the candidate genes using the "glmnet" package. Cross-validation was employed to select the

penalty parameter λ, which helped select relevant genes and reduce model complexity. A multivariate regression analysis of the candidate genes was conducted using the "survival" package to construct the prognostic model.

Risk score = $\Sigma_{i=1}^{n}\beta i \times Expi$. βi is the risk coefficient, and *Expi* is the gene expression level.

Based on this model, a risk score for each patient was calculated using the expression levels and risk coefficients of the genes, and patients were categorized into high- and low-risk groups according to the median score. Survival curves were generated based on the risk scores. The "timeROC" package was used to plot receiver operating characteristic (ROC) curves and calculate the area under the curve (AUC) values for 1-year, 3-year, and 5-year survival rates. Additionally, score distribution plots, survival status distribution plots, and heatmaps of expression levels were created for the high- and low-risk groups.

Construction of a nomogram for independent prognostic analysis

We conducted univariate and multivariate regression analyses on the training set samples, integrating clinical information and prognostic risk scores, and generated corresponding forest plots. Utilizing the "rms" package, we constructed a nomogram to predict patient survival probabilities at 1, 3, and 5 years. Calibration curves and decision curve analysis (DCA) were subsequently performed to assess the predictive performance of the nomogram and to establish its role as an independent prognostic factor. Furthermore, we validated the predictive accuracy of the nomogram using calibration curves derived from the independent dataset GSE21257.

Immunological evaluation

We employed the "GSVA" and "estimate" packages to conduct ssGSEA analysis, quantifying the extent of immune cell infiltration. Violin plots were generated to illustrate immune scores, stromal scores, ESTIMATE scores, and tumor purity for both high- and low-risk groups. Box plots were created to statistically compare the expression levels of immune checkpoints and the degree of immune cell infiltration between these groups. The Tumor Immune Phenotype (TIP) (http://biocc.hrbmu.edu.cn/TIP/) is a web-based analysis platform designed to assess the activation levels of the seven steps in the anti-cancer immune cycle [23]. We evaluated the associations between the activation levels of this immune cycle and risk scores, along with characteristic genes. Furthermore, we used the ssGSEA algorithm, TIMER algorithm, and MCP-Counter to analyze the relationships between characteristic genes and immune cells.

Investigation of biological functions and active pathways

Differential analysis was performed between the high-risk and low-risk groups of OSA using the edgeR package (|logFC|>1, $p < 0.05$). GO and KEGG enrichment analyses were conducted on the differentially expressed genes using the "clusterProfiler" package and "GOplot."

Analyzing the efficacy of risk scores in predicting immune therapy response

Anti-PD-1 and anti-PD-L1 checkpoint inhibitor therapies have emerged as significant components of immunotherapy, garnering considerable attention [24]. To assess the ability of risk scores to predict responses to immune checkpoint blockade, we gathered transcriptomic and clinical data from patients receiving anti-PD-L1 treatment within the IMvigor210 cohort (Supplementary Table SIV). Utilizing the risk scores, we categorized the samples into high-risk and low-risk groups.

Single-cell sequencing analysis based on OSA

This study employed the Read10X function from the "Seurat" package to analyze gene expression data from 11 samples in GSE152048. We identified the top 2,000 highly variable genes using the FindVariableFeatures function, and removed batch effects through anchor-based data integration with the FindIntegrationAnchors function. Low-quality cells, defined as those with fewer than 300 detected genes or exhibiting more than 10% mitochondrial gene expression, were excluded, and the remaining cells were normalized. Using the "SCISSOR" package, we categorized cells into high-risk and low-risk groups based on patient expression data and risk stratification information from TARGET-OS. Finally, we analyzed and visualized the intercellular communication network within the TME using the "CellChatR" package.

Potential drug targets and prediction of drug inhibitory concentrations

The present study aimed to identify potential therapeutic targets and agents. We utilized the CellMiner database (https://discover.nci.nih.gov/cellminer/) to screen for antitumor drugs significantly associated with drug sensitivity and the expression of prognostic genes. Additionally, we explored the DGIdb database (https://www.dgidb.org) to identify approved drugs that interact with the feature genes, discussing the potential drug

targets and mechanisms linked to disease susceptibility genes. The "pRRophetic" package was employed to predict the half-maximal inhibitory concentration (IC_{50}) of various drugs in high-risk and low-risk groups. A lower IC_{50} indicates greater effectiveness of the drug in tumor treatment.

Cell acquisition and cell culture

hFOB1.19, SAOS2 and U2OS cell lines were obtained from the American Type Culture Collection (ATCC) and cultured in DMEM. All cell cultures were maintained in a 37°C incubator with 5% CO_2.

RNA isolation and quantitative real-time PCR (qRT-PCR)

Total RNA was extracted from cells using RNAiso Trizol reagent (Sangon Biotech, China). cDNA was synthesized through reverse transcription with the GeniuSaript III Select RT Kit for qPCR (Youji, China). For qRT-PCR, the uGreener Fex qPCR 2X MiX (Youji, China) was utilized on the LightCycler 480 qPCR system (Roche, Switzerland), with the primer sequences listed below. The results were normalized to GAPDH, and relative expression levels were calculated using the $2^{-\Delta\Delta CT}$ method (Table I).

Cytotoxicity assay

The 3-(4,5-dimethylthiazol-2-yl)-2,5-diphenyltetrazolium bromide (MTT) method was used to determine the toxic effects of drugs on cells. U2OS and SAOS2 cells were seeded into a 96-well plate. After cell attachment, the cells were treated with various concentrations of temozolomide or cisplatin for 48 h, including a blank control group. Subsequently, 10 µl of MTT solution was added to each well and the plate was incubated at 37°C for 2 h. The supernatant was then aspirated, and DMSO was added to dissolve the formazan. The absorbance of each well was measured at a wavelength of 490 nm.

Cell apoptosis assay

Terminal deoxynucleotidyl transferase (TdT) dUTP nick-end labeling (TUNEL) assay was used to assess the effect of drugs on cell apoptosis. U2OS and SAOS2 cells were seeded onto culture plates containing coverslips. After cell attachment, cells were treated with temozolomide or cisplatin for 48 h, including a solvent control group. Following treatment, TUNEL staining was performed: cells were fixed with 4% paraformaldehyde, permeabilized with 0.1% Triton X-100, incubated with TUNEL reaction mixture to label DNA fragmentation, and counterstained with DAPI. After washing, coverslips were mounted with antifade mounting medium and observed under a fluorescence microscope. Multiple fields of view were randomly selected, and the numbers of TUNEL-positive and DAPI-positive cells were counted to calculate the apoptosis rate.

Results

Identification of CMRGs linked to OSA and development of molecular subtypes from DECMRGs

This study initially conducted a differential analysis of the normal and OSA groups in the GSE99671 dataset (Normal: 18, OSA: 18) with criteria set at $|logFC| > 0.585$ and $p < 0.05$, resulting in 1,046 upregulated and 1,365 downregulated genes (OSA-DEGs, Figure 1 A). By intersecting OSA-DEGs with CMRGs, we identified 13 differentially expressed CMRG-related genes (DECMRGs, Figure 1 B). A PPI network was constructed for the 13 DECMRGs using the STRING database, as illustrated in Figure 1 C, revealing strong interactions among CTLA4, TNFRSF4, CD86, CD276, and CD28. The expression levels of DECMRGs in both the normal and OSA groups were analyzed, and a heatmap was generated, indicating that CTLA4, TNFRSF4, CD86, CD276, and CD28 were significantly overexpressed in the OSA group (Figure 1 D).

The objective of this study was to conduct a comprehensive analysis of the key characteristics of OSA tissues to inform the design of personalized treatment strategies for OSA patients. To accomplish this, we used NMF clustering techniques to classify the TARGET-OS samples into three subtypes based on DECMRGs (Sample: Cluster 1: 26, Cluster 2: 13, Cluster 3: 46, Figure 1 E). K-M curve analysis demonstrated significant

Table I. Primer sequences used for quantitative real-time PCR (qRT-PCR)

Gene name	Forward primer sequence (5′-3′)	Reverse primer sequence (5′-3′)
EPYC	AGGTCAGAGCCAAAGGAAAGC	TAGAGTTGGGGCAGTCACAG
SCD1	TTCCCGACGTGGCTTTTTCT	AGCCAGGTTTGTAGTACCTCC
AOC3	CAAGTGTCAGAGCACACCCT	TCCAGTCCTGCTACATCCAGA
MYC	TGGAAAACCAGCCTCCCG	TTCTCCTCCTCGTCGCAGTA
KLK2	TGGAGGGGAAAGGGTGATTC	CCACTTCCGGTAATGCACCA
GAPDH	ACATCGCTCAGACACCATG	TGTAGTTGAGGTCAATGAAGGG

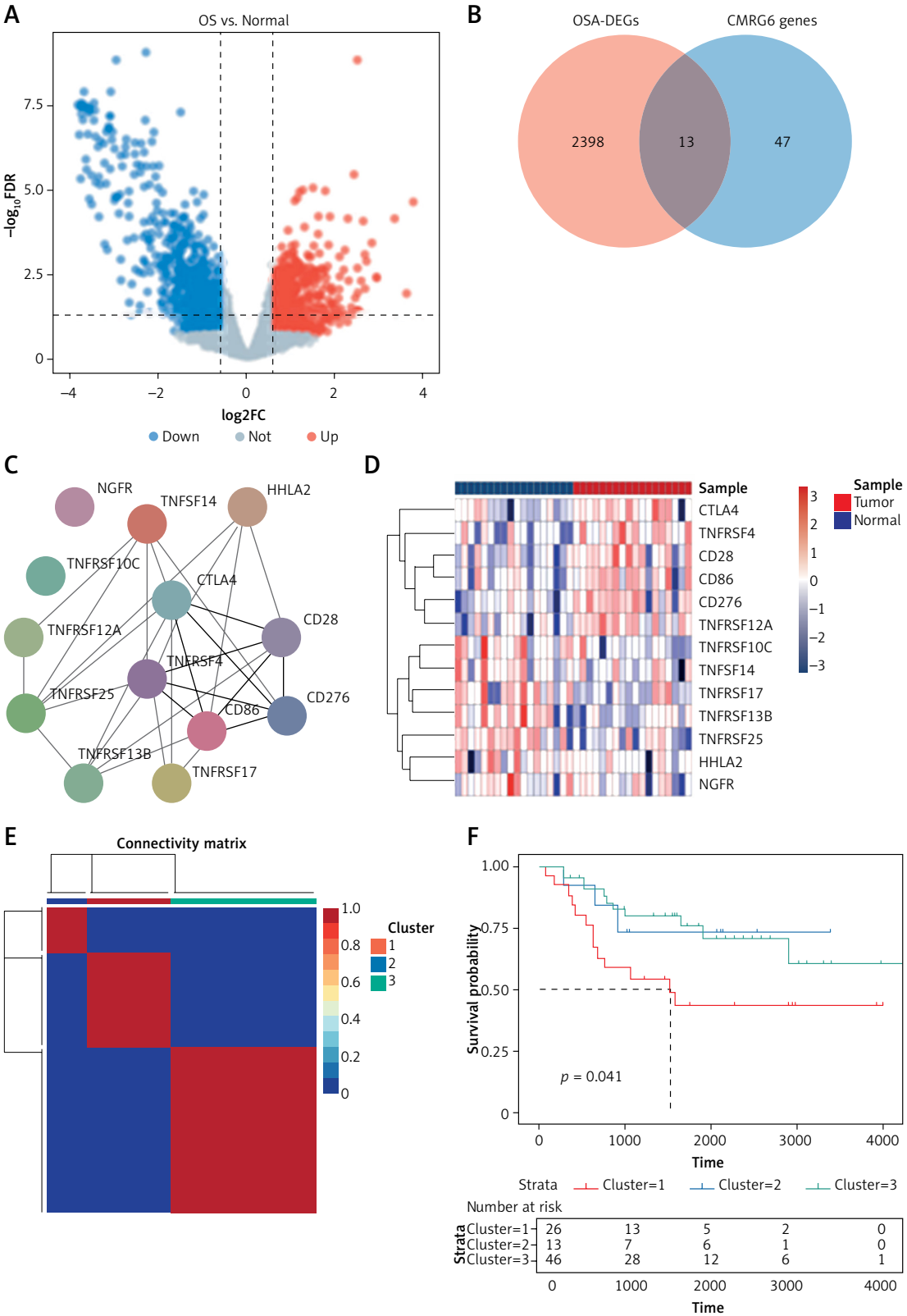


Figure 1. Identification of prognostic candidate genes and subtype construction. **A** – Volcano plot depicting the expression of differentially expressed genes between normal tissue and OSA tissue, (upregulated: 1046, down-regulated: 1365). **B** – Venn diagram showing the intersecting genes between OSA-DEGs and CMRGs gene sets. **C** – Results of the PPI network diagram for the 13 DECMRGs. **D** – Heatmap showing the differences in expression of the 13 DECMRGs in normal and OSA tissues. **E** – NMF clustering results show that the optimal number of clustering results is 3. **F** – KM curve analysis describes the survival outcomes for the three subgroups of patients, with those in subtype 1 having the poorest survival

differences in survival outcomes among the three subtypes, with Cluster 1 showing the poorest survival rates (Figure 1 F).

Analysis of immune function and immune cell infiltration among molecular subtypes based on DECMRGs

To explore the differences in immune-related functions and immune cell infiltration among the three subtypes, we conducted ssGSEA analysis to evaluate immune cell infiltration across these subtypes (Figure 2 A). Our findings indicate that subtype 3 exhibited significantly higher levels of immune cell infiltration compared to subtypes 1 and 2. The results illustrated in Figures 2 B and C further confirm that immune cell infiltration is notably more pronounced in subtype 3. Furthermore, stromal score comparisons revealed that subtype 3 had a significantly higher stromal score than subtype 1 (p = 0.0085). In contrast, subtype 1 exhibited significantly higher tumor purity than subtype 3 (p = 0.049), while its ESTIMATE score was significantly lower than that of subtype 3 (p = 0.049) (Figure 2 D).

Differential analysis and biological function exploration among subtypes

We analyzed DECMRG expression across the three subtypes and found that TNFRSF12A showed the lowest expression in subtype 1, while NGFR was significantly higher in subtype 2 compared to the other subtypes. Additionally, CD276 was most highly expressed in subtype 1, and TNFRSF10C was most highly expressed in subtype 3 (Figure 3 A). To further investigate the clinical characteristics of the 3 patient subtypes, we conducted a statistical analysis of disease metastasis. As shown in Figure 3 B, the metastasis rates were 23% in subtype 1, 15% in subtype 2, and

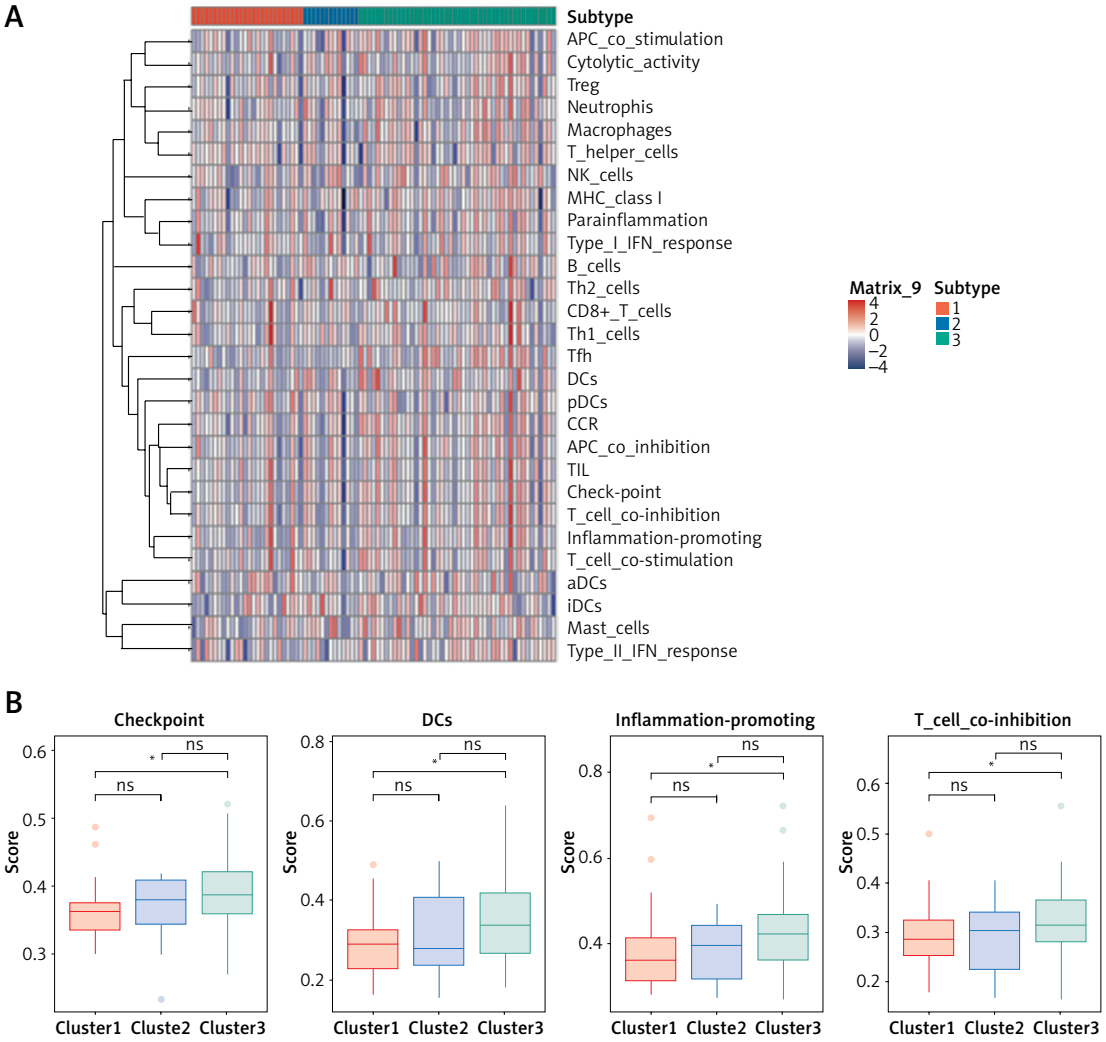


Figure 2. Analysis of immune function and immune infiltration. **A** – Heatmap depicting the differences in immune cell infiltration in the three subtypes groups. **B** – Box plots showing analysis of differences in the degree of infiltration of each immune cell in the three subtyping groups. ns denotes no significant difference, *signifies $p < 0.05$, **represents $p < 0.01$, and ***corresponds to $p < 0.001$

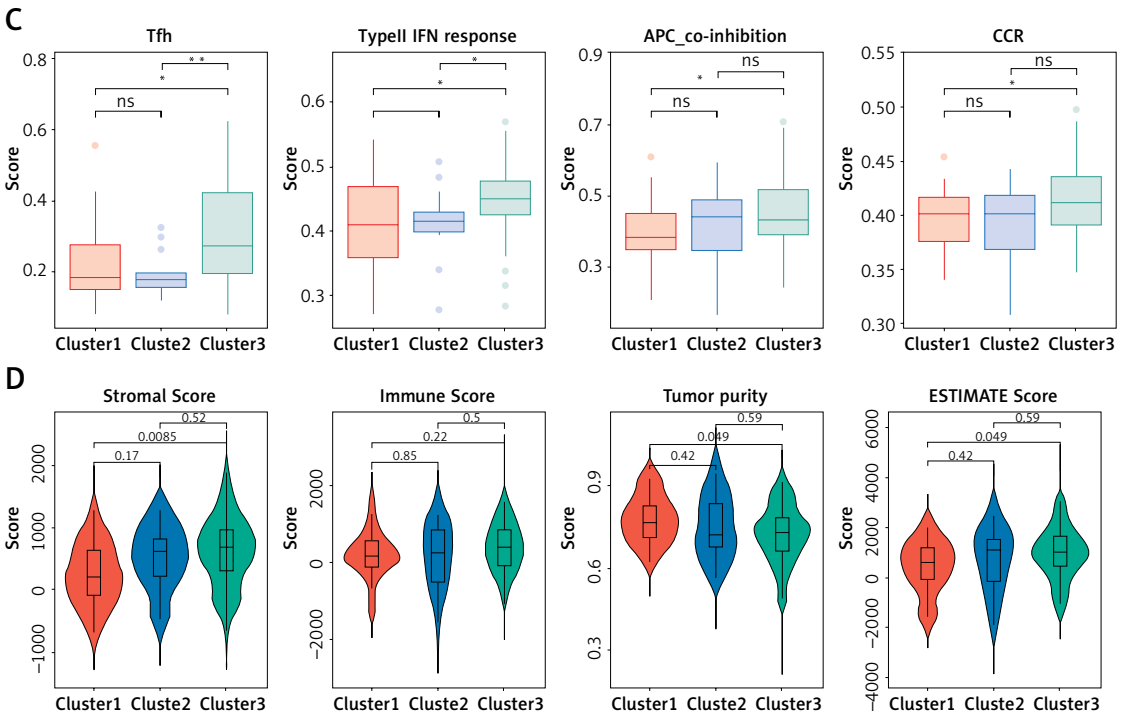


Figure 2. Cont. **C** – Variations in immune cell infiltration among the three subtypes. **D** – Violin plot illustrating the findings related to the stromal score, immune score, tumor purity, and ESTIMATE score across the three subtypes. ns denotes no significant difference, *signifies $p < 0.05$, **represents $p < 0.01$, and ***corresponds to $p < 0.001$

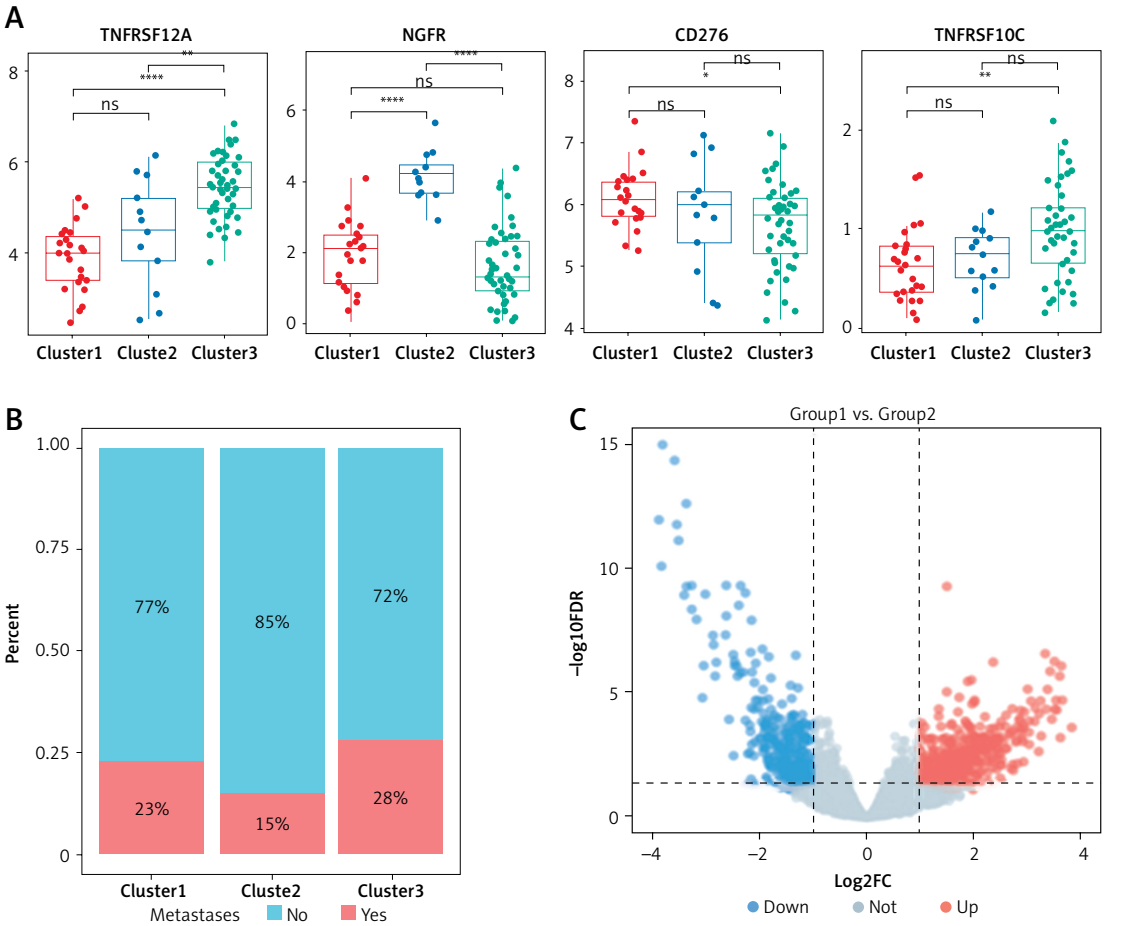


Figure 3. Analysis of differences between subtypes and functional exploration. **A** – Analysis of DECMRG expression among subtypes. Expression levels are plotted on the vertical axis, while the horizontal axis represents the different subtypes. **B** – Metastasis of illness in patients with various subtypes. **C** – Volcano plot showing the number of differentially expressed genes between the merged subtypes (subtype 2 and 3) and subtype 1, upregulated genes: 802, downregulated genes: 385. ns indicates no significant difference, *indicates significant difference, ** and *** indicate increasing levels of statistical significance

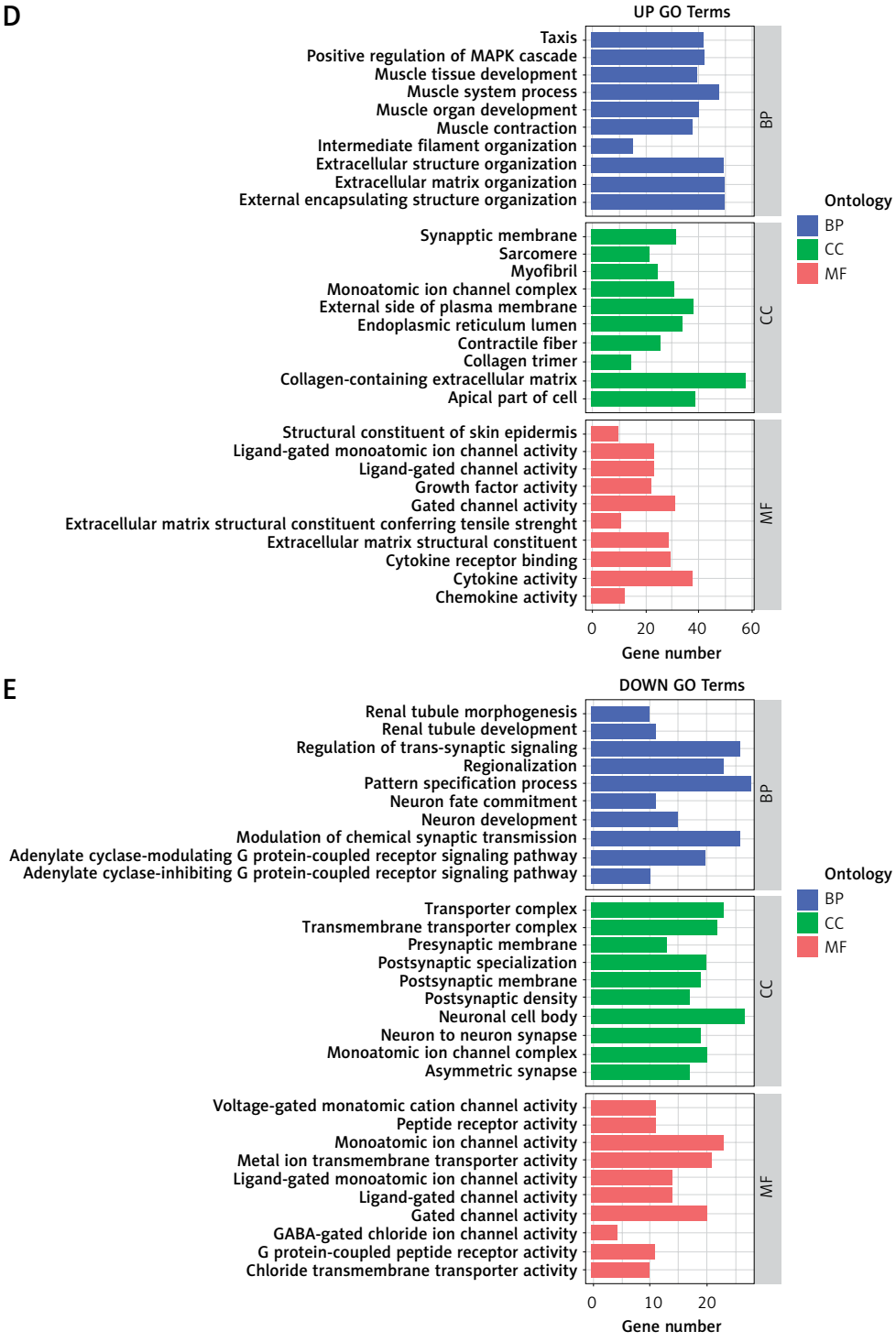


Figure 3. Cont. **D** – Results of GO enrichment analysis of upregulated genes. **E** – Results of GO enrichment analysis of downregulated genes. ns indicates no significant difference, *indicates significant difference, ** and *** indicate increasing levels of statistical significance

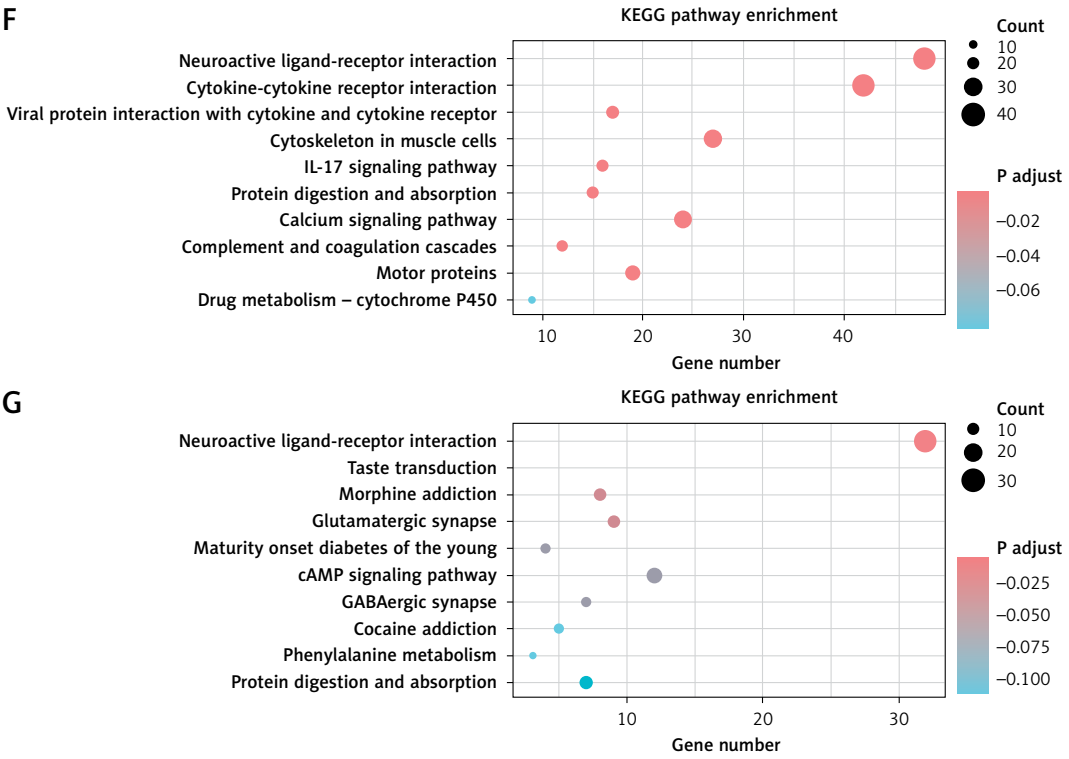


Figure 3. Cont. **F** – KEGG enrichment analysis of upregulated genes. **G** – Outcomes of KEGG enrichment analysis of downregulated genes. ns indicates no significant difference, *indicates significant difference, ** and *** indicate increasing levels of statistical significance

28% in subtype 3. To explore differences between the subtypes, we merged the data from subtypes 2 and 3 based on survival outcomes. We then performed a differential analysis of the combined gene set compared with subtype 1, using thresholds of log|FC| > 1 and $p < 0.01$. This yielded 1,187 differentially expressed genes (group-DEGs), including 802 upregulated and 385 downregulated genes (Figure 3 C). Subsequently, we conducted GO and KEGG analyses to further explore the biological functions and pathway activities associated with the groups-DEGs. As illustrated in Figure 3 D, upregulated genes were enriched in extracellular structure and muscle tissue-related processes. In contrast, downregulated genes were mainly associated with neuroregulation, transmembrane transport, and protein function (Figure 3 E). KEGG analysis showed that upregulated genes were significantly involved in neural activity regulation, inflammatory signaling, and protein metabolism-related pathways (Figure 3 F), while downregulated genes were primarily enriched in protein metabolism-related pathways (Figure 3 G).

Identification of prognosis-related feature genes for developing OSA prognosis models

To further analyze the prognostic characteristics of OSA, this study identified the intersection of the OSA-DEGs gene set and the group-DEGs gene set, resulting in 274 overlapping genes (Figure 4 A). Subsequently, univariate Cox analysis was performed, which yielded 54 genes significantly associated with survival ($p < 0.05$) (Figure 4 B). LASSO regression analysis was then employed to refine the list of candidate genes (Figure 4 C). Based on cross-validation results, we selected an optimal model with 13 genes (Figure 4 D). Further multivariate regression analysis resulted in the selection of 5 characteristic genes to construct the prognostic model: risk score = –0.3182*EPYC + 0.2907*SCD1 + 0.5353*AOC3 + 0.6530*MYC + 2.0331*KLK2 (Figure 4 E). To evaluate model performance, ROC curves were plotted. As shown in Figure 4 F, the AUC values for the training set were 0.895 (1 year), 0.834 (3 years), and 0.862 (5 years). For the validation set, the AUCs were 0.719, 0.714, and 0.698 at the respective time points (Figure 4 G). These results indicate good predictive performance in the training set and moderate predictive performance in the validation set. Based on the median risk score, OSA patients were classified into low-risk and high-risk groups. As illustrated in the KM curve results in Figure 4 H, the survival probability of patients in the low-risk group was significantly higher than that of the high-risk group ($p < 0.0001$). Additionally, survival status and risk scores were more favorable in the low-risk group (Figure 4 I). Among the feature genes,

SCD1, MYC, AOC3, and KLK2 were overexpressed in the high-risk group, while EPYC was expressed at lower levels (Figure 4 J).

Constructing a nomogram for independent prognostic analysis

Survival analysis of the feature genes revealed that while EPYC showed a survival trend, the difference was not statistically significant (p = 0.05384, Figure 5 A). In contrast, MYC exhibited a significant difference between risk groups (Figure 5 B). We then performed univariate and multivariate regression analyses integrating clinical features and risk scores, identifying M stage and risk score as independent prognostic factors (p < 0.05, Figures 5 C, D). To facilitate clinical application, we developed a nomogram integrating

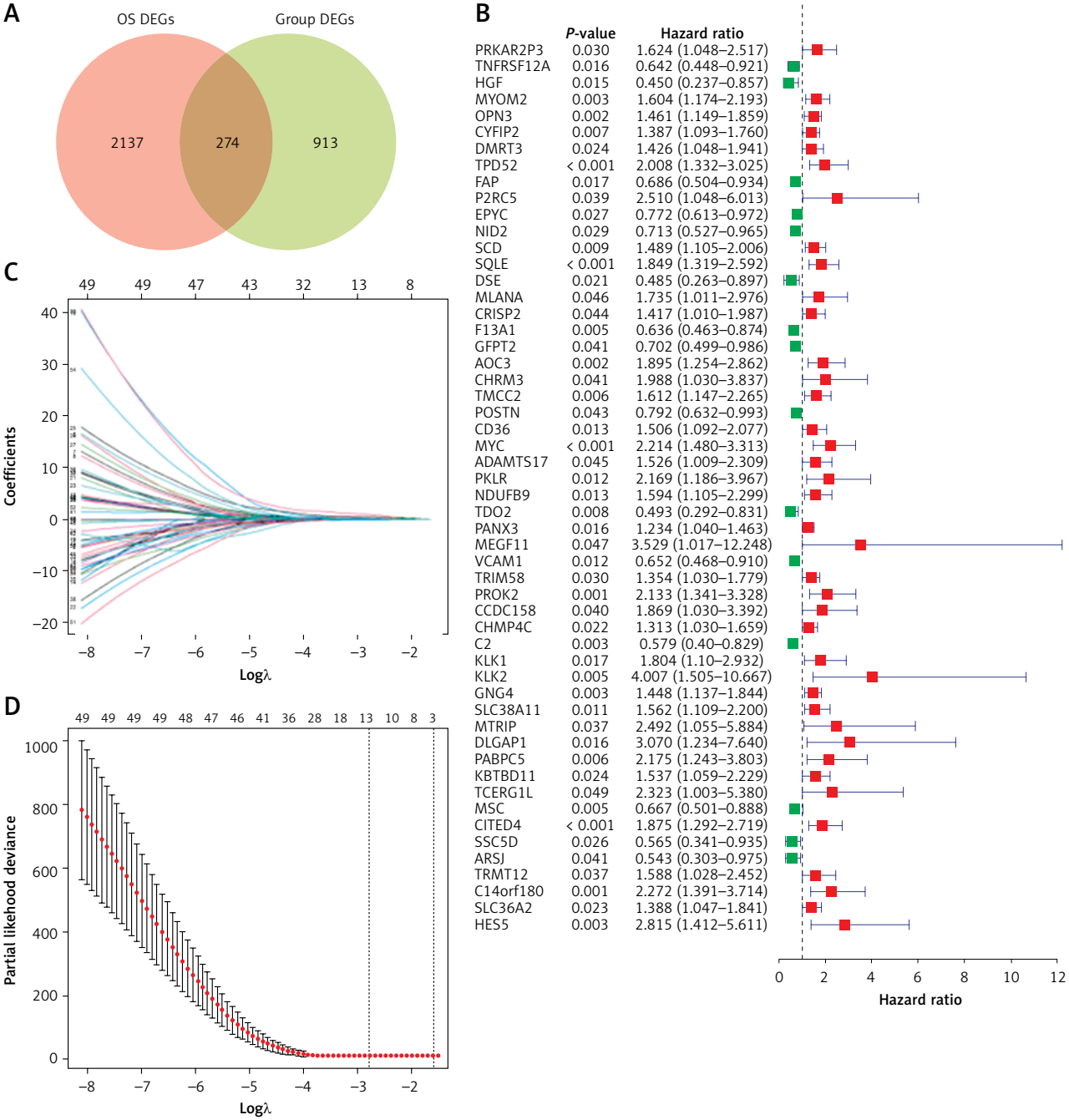


Figure 4. Identification of characteristic genes and construction of prognostic models. **A** – Venn diagram representing the intersection of the OSA-DEGs gene set and the group-DEGs gene set, with 274 intersecting genes. **B** – Results of the univariate regression analysis showing genes with a significance level less than 0.05. **C** – LASSO regression coefficient path plot showing each line representing a variable, with the vertical axis indicating coefficient values and the horizontal axis representing log(λ) values. **D** – Cross-validation curve of the LASSO regression showing the partial likelihood deviance across different values of log(λ)

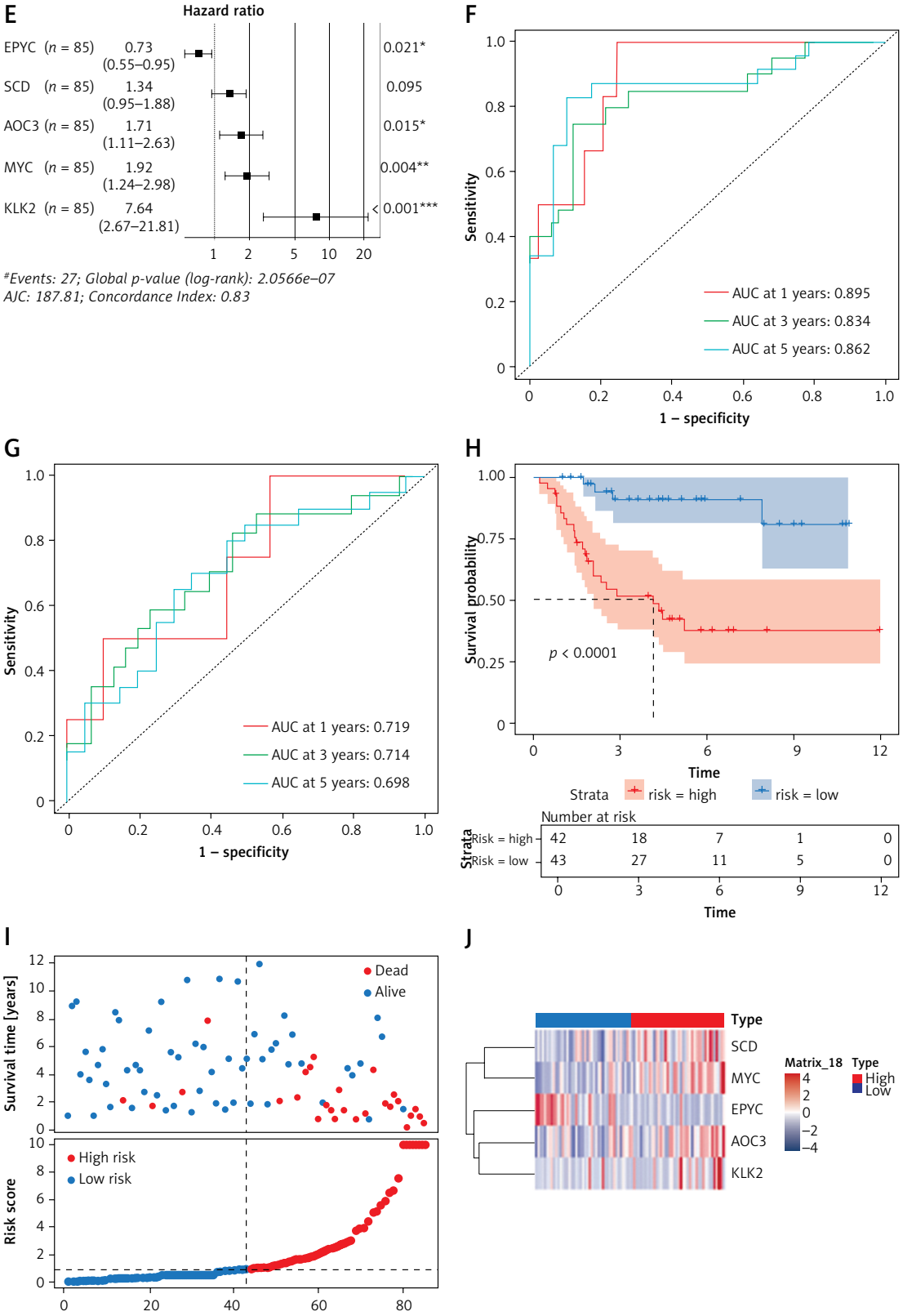


Figure 4. Cont. **E** – Results of the multivariate regression analysis identifying 5 characteristic genes. **F** – ROC analysis results for the training set indicating AUC values of 0.895, 0.834, and 0.862 at 1, 3, and 5 years, respectively. **G** – AUC values of the ROC curve for the validation set are 0.719, 0.714, and 0.698 at 1, 3, and 5 years, respectively. **H** – KM curve showing that the survival outcomes of the low-risk group are more favorable than those of the high-risk group. **I** – Distribution of survival status and risk scores for the high-risk and low-risk groups. **J** – Heatmap showing the expression levels of characteristic genes in the two risk groups

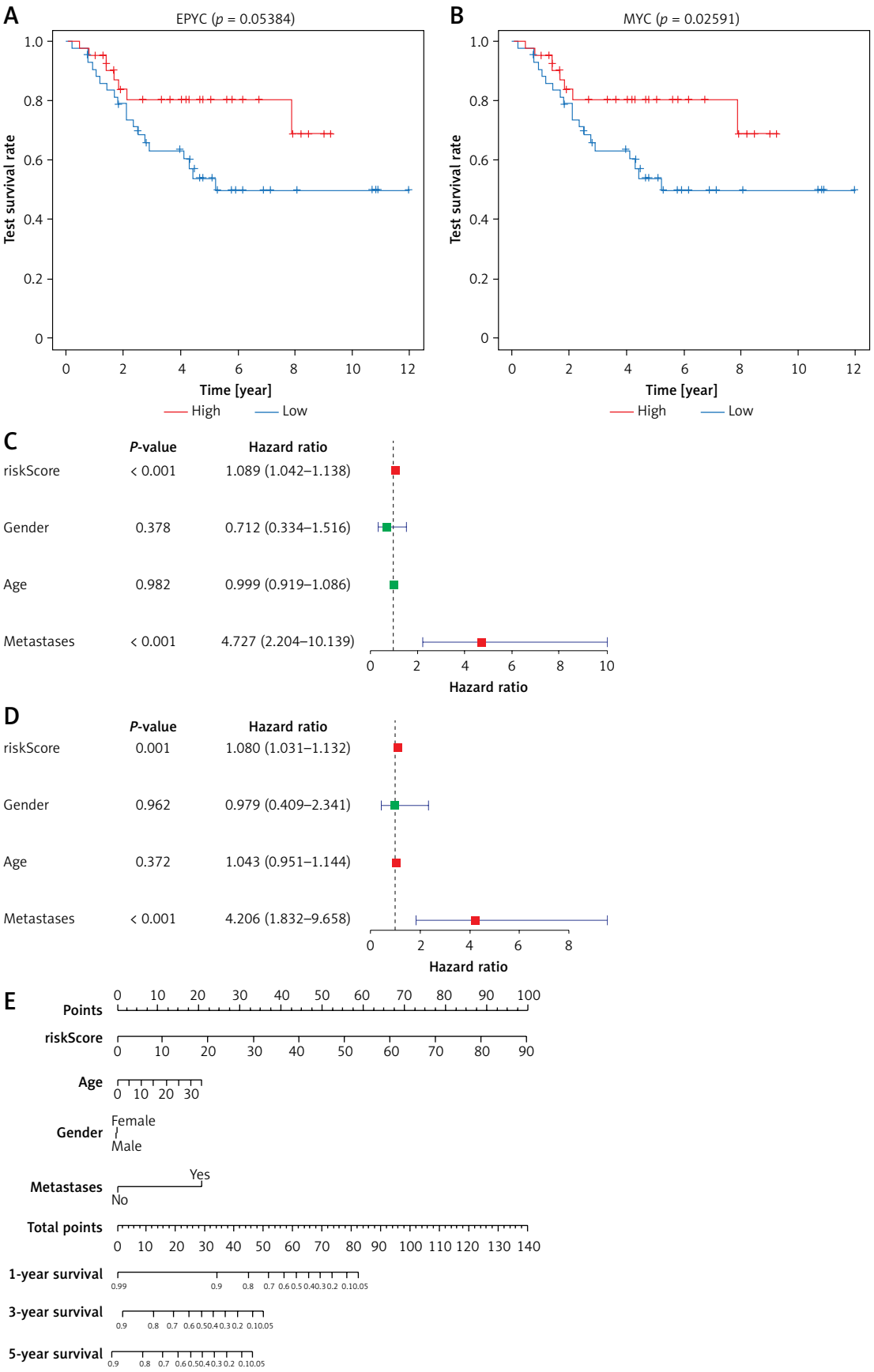
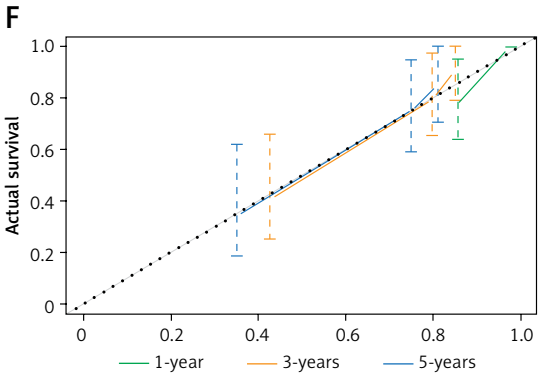
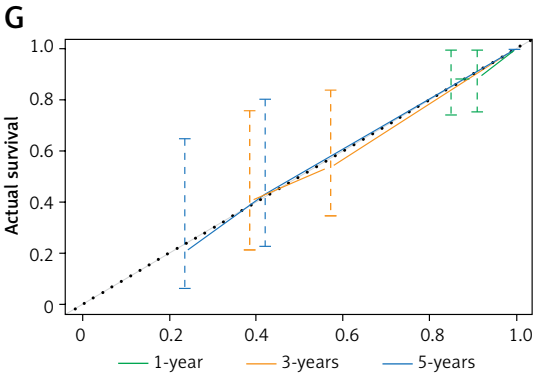


Figure 5. Development and assessment of nomograms. **A** – KM curve for EPYC. **B** – The KM curve illustrates a higher survival rate for MYC in the low-risk category compared to the high-risk category, p =0.02591. **C** – Results of univariate regression analyses utilizing risk scores and clinical data. **D** – Results of multivariate regression analyses based on risk score and clinical information. **E** – Nomogram for comprehensively assessing the prognostic performance of OSA



N = 85; d = 27 p = 4, 28.3333333333333 subjects per group. Nomogram-predicted probability of survival. Gray: ideal
X – resampling optimism added, B = 40. Based on observed-predicted.



N = 53; d = 23 p = 4, 17.6666666666667 subjects per group. Nomogram-predicted probability of survival. Gray: ideal
X – resampling optimism added, B = 4. Based on observed-predicted.

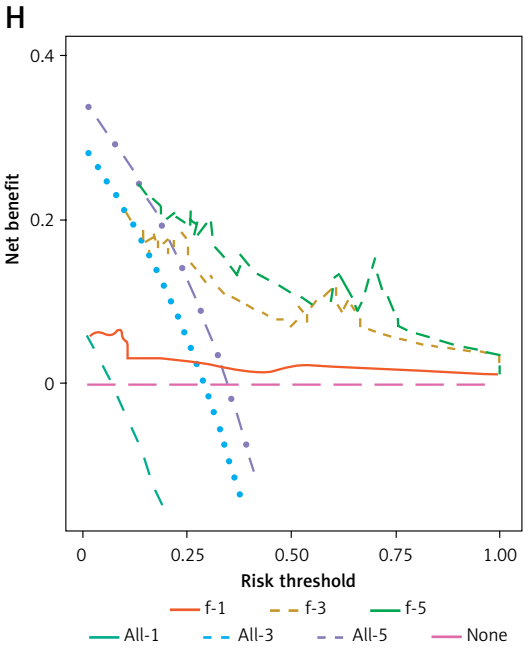


Figure 5. Cont. **F** – Calibration curves for 1-, 3-, and 5-year survival in the training dataset. **G** – Calibration curves for 1-, 3-, and 5-year survival in the validation dataset, showing the relationship between nomogram-predicted and observed survival. **H** – Results of DCA at 1, 3, and 5 years; the horizontal axis illustrates the threshold probability, whereas the vertical axis reflects the net benefits achieved

risk score and clinical variables to predict 1-, 3-, and 5-year survival (Figure 5 E). Calibration curves (Figure 5 F) showed that the nomogram's predicted outcomes closely matched observed survival in the training set. Similar results were observed in the validation set (Figure 5 G). Decision curve analysis (DCA) further demonstrated that the nomogram provided potential net clinical benefit for predicting survival at 1, 3, and 5 years (Figure 5 H). In summary, our findings suggest that the nomogram has good predictive performance, and the 5-gene-based model may serve as an independent prognostic indicator for OSA.

Examination of the immune environment between high-risk and low-risk groups

To comprehensively assess immune infiltration and prognosis across risk groups, ssGSEA was used to compare immune-related functions and cell infiltration between high- and low-risk groups. As shown in Figure 6 A, immune infiltration was markedly higher in the low-risk group. Figure 6 B further supports this finding, with box plots demonstrating elevated infiltration levels for most immune cell types. Consistently, the low-risk group showed significantly higher ESTIMATE, immune, and stromal scores, while tumor purity was increased in the high-risk group (Figure 6 C). Metastasis rates were also lower in the low-risk group (Figure 6 D).

Immune checkpoint gene expression was broadly upregulated in the low-risk group (Figure 6 E). Correlation analysis revealed that AOC3 and EPYC were positively associated with B cells, while MYC showed a negative correlation. Similarly, AOC3 and KLK2 positively correlated with pDCs, whereas MYC was negatively correlated. AOC3 (Figure 6 F), KLK2 (Figure 6 G), and EPYC (Figure 6 H) were positively correlated with most immune

cells, while MYC (Figure 6 I) and SCD1 (Figure 6 J) showed negative correlations.

To investigate interactions with oncogenic pathways, we analyzed the expression correlation between canonical oncogenes and signature genes in the TARGET-OS cohort. As shown in Supplementary Figure S1, KLK2 was negatively correlated with FAS (r = –0.41, p < 0.01), and SCD1 positively correlated with NRAS (r = 0.32, p < 0.01), indicating potential associations be-

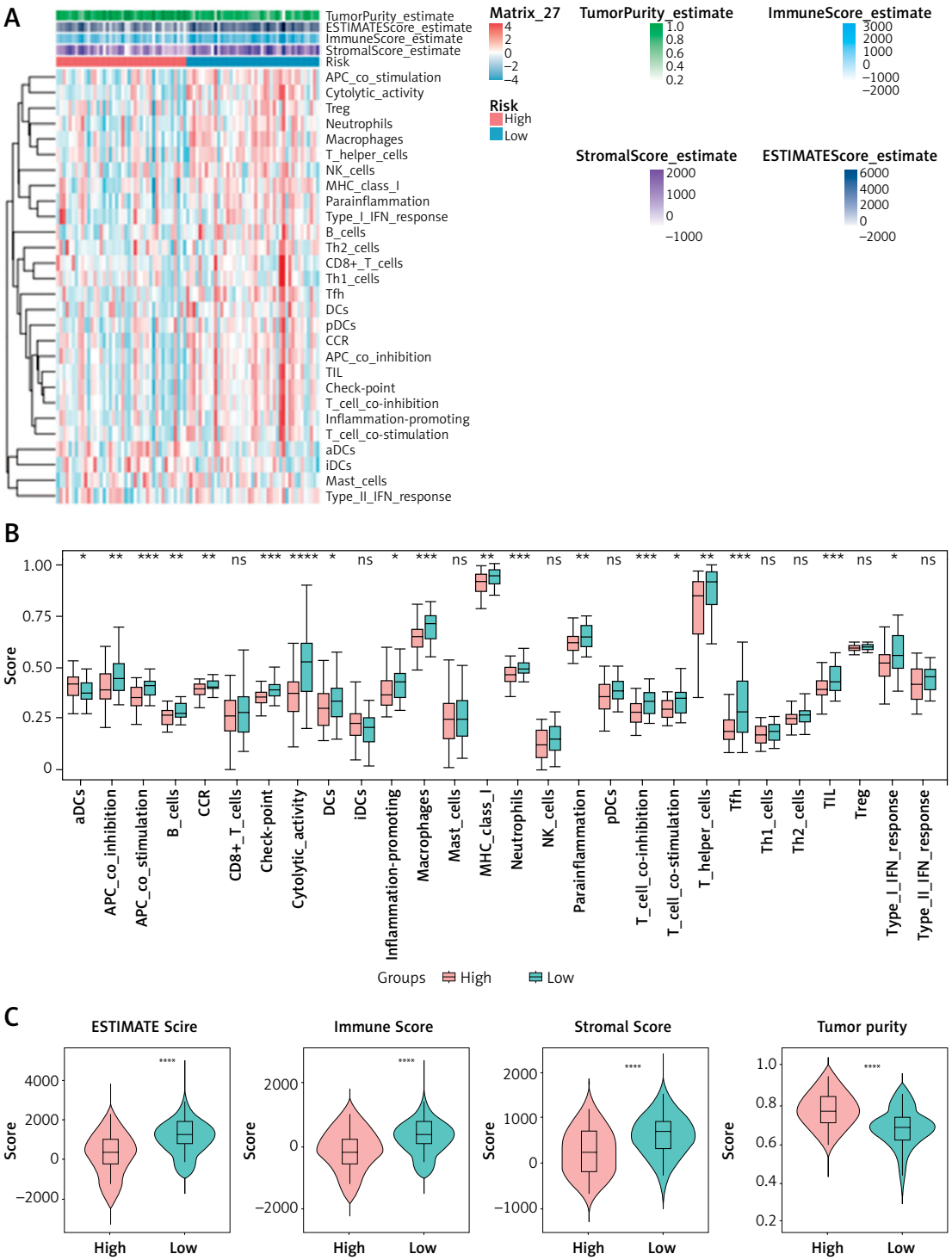


Figure 6. Evaluation of immune activity and infiltration of immune cells across the two risk categories. **A** – Heatmap displaying variations in immune cell infiltration between the two risk groups. **B** – Box plots illustrating variations in immune cell infiltration expression between the two risk groups. **C** – Violin plot illustrating the variation in multiple scores across the two risk groups. ns denotes no significant difference, *signifies p < 0.05, **represents p < 0.01, and ***indicates p < 0.001

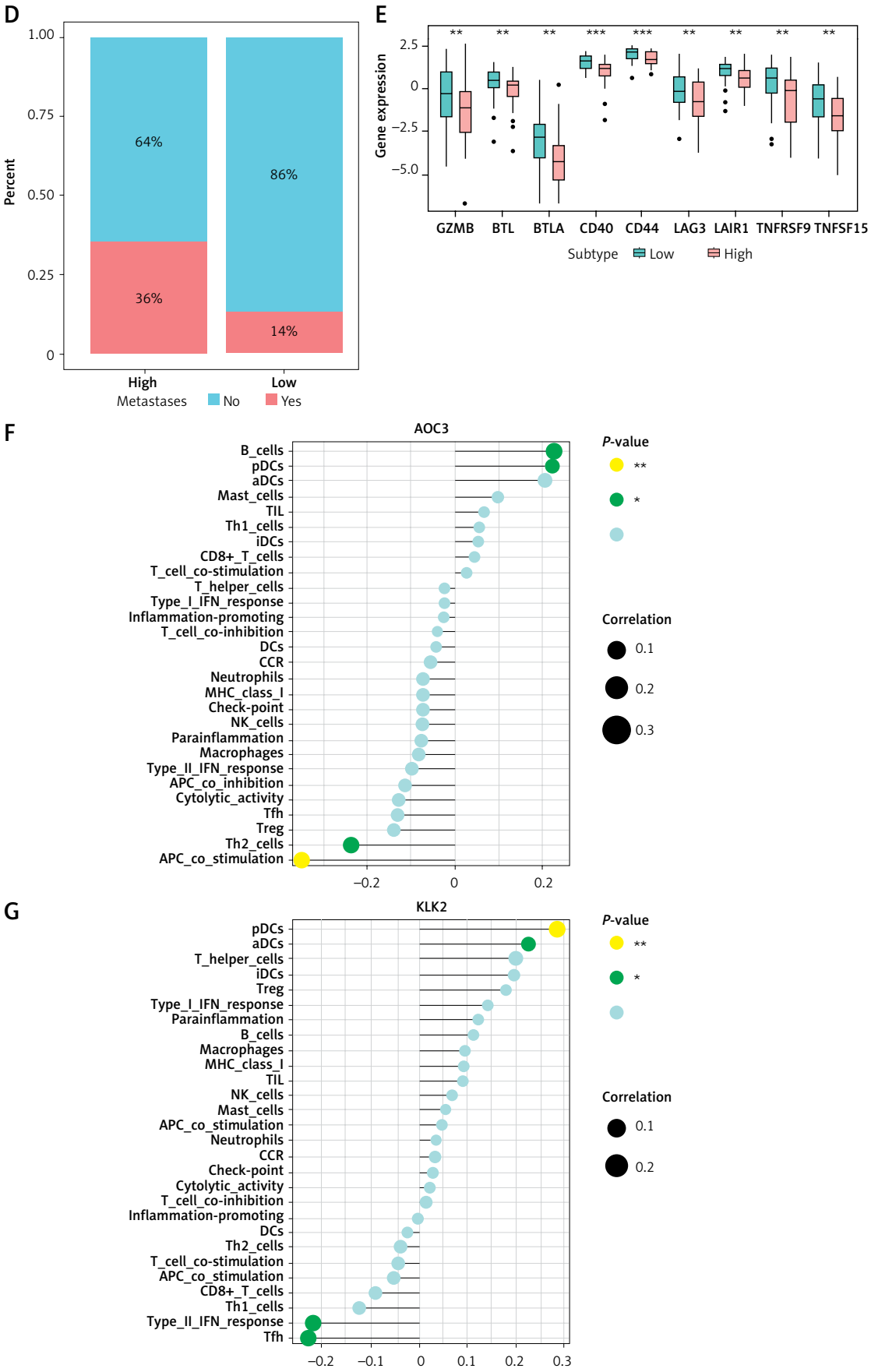


Figure 6. Cont. **D** – Comparison of disease metastasis between high- and low-risk groups. **E** – Comparison of immune checkpoint gene expression in high-risk versus low-risk groups. Correlation analysis diagram of characteristic genes AOC3 (**F**), KLK2 (**G**). ns denotes no significant difference, *signifies $p < 0.05$, **represents $p < 0.01$, and ***indicates $p < 0.001$

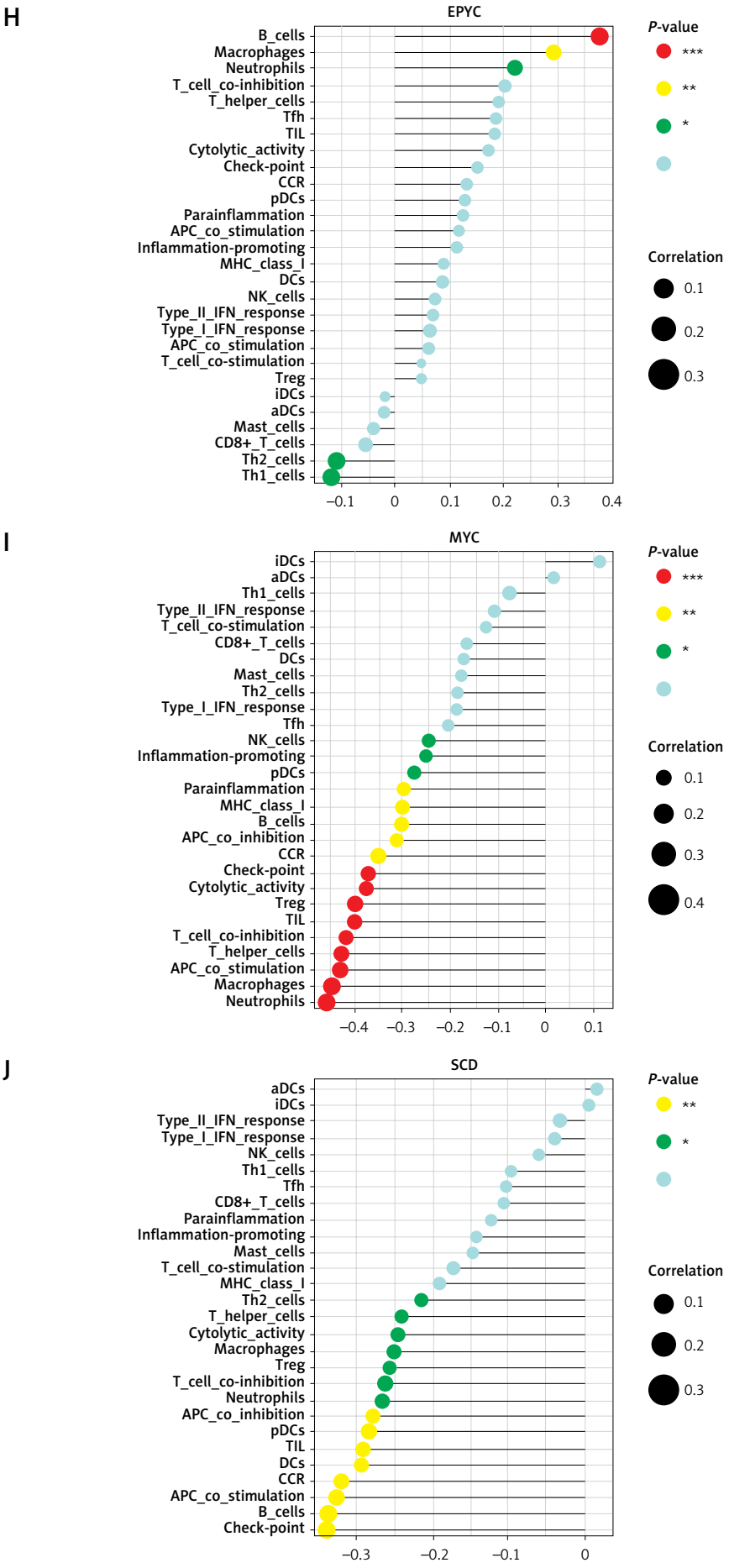


Figure 6. Cont. Correlation analysis diagram of characteristic genes EPYC (**H**), MYC (**I**), and SCD1 (**J**) with immune cell infiltration. ns denotes no significant difference, *signifies $p < 0.05$, **represents $p < 0.01$, and ***indicates $p < 0.001$

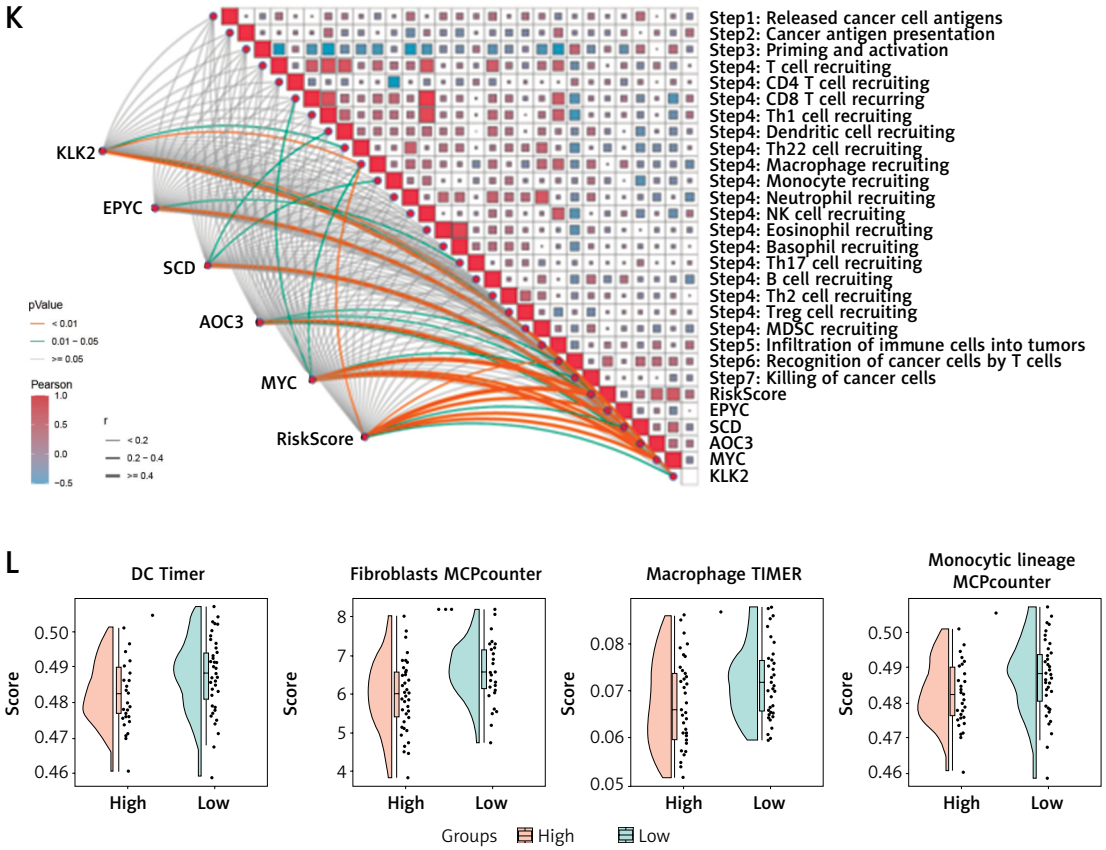


Figure 6. Cont. **K** – Heatmap of the association between signature genes, risk scores, and the immunization cycle. **L** – Infiltration levels for various cell types, such as dendritic cells (DC), fibroblasts, macrophages, and cells from the monocytic lineage, were compared between high-risk and low-risk groups. ns denotes no significant difference, *signifies $p < 0.05$, **represents $p < 0.01$, and ***indicates $p < 0.001$

tween CMRG-derived markers and oncogenic signaling in osteosarcoma.

We further evaluated the association between the risk score and the tumor immune cycle. As illustrated in Figure 6 K, the risk score and most characteristic genes were negatively correlated with step 4 (immune cell recruitment). Additionally, Figure 6 L shows that infiltration scores for immune and tissue repair cells were significantly higher in the low-risk group.

Overall, these findings indicate a more active immune microenvironment in low-risk patients, suggesting that these patients may be more responsive to immunotherapy.

Response to PD-L1 inhibition immunotherapy according to risk scores

Following the assessment of immune infiltration, we extracted data from the IMvigor210 cohort regarding responses to PD-L1 inhibitor immunotherapy from public databases. In this cohort of 348 patients, responses to PD-L1 blockade varied and included stable disease (SD), partial response (PR), complete response (CR), and disease progression (PD). Our analysis using KM curves demonstrated that the survival outcomes for the low-risk group were significantly better than those of the high-risk group (Figure 7 A). Importantly, we classified SD and PD as NR (not responding) and CR and PR as R (responding). The analysis indicated that patients in the R group exhibited significantly lower risk scores compared to those in the NR group (Figure 7 B). Additionally, the proportion of NR patients in the low-risk group was significantly lower than that in the high-risk group (Figure 7 C).

Functional enhancement of differentially expressed genes in high- and low-risk cohorts

To further investigate the biological functions and underlying molecular mechanisms across risk groups, we conducted differential expression analysis between the high- and low-risk groups ($|\log FC| > 1$, $p < 0.05$, Figure 8 A). This analysis identified 908 upregulated and 413 downregulated genes, which were subsequently subjected to GO and KEGG enrichment analyses. GO analysis revealed that differentially expressed genes were significantly enriched in cell membrane structure-related pathways within the Biological Pro-

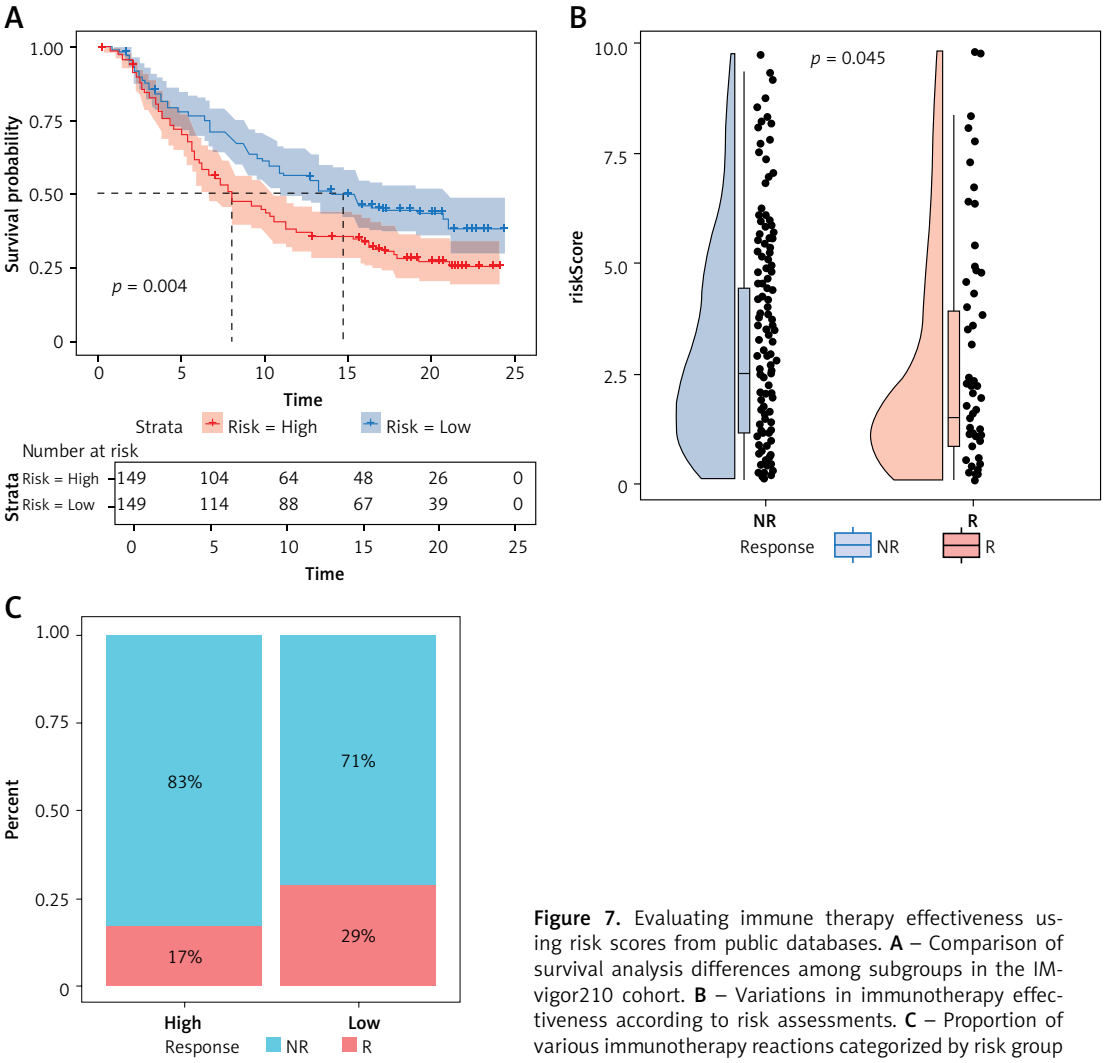


Figure 7. Evaluating immune therapy effectiveness using risk scores from public databases. **A** – Comparison of survival analysis differences among subgroups in the IMvigor210 cohort. **B** – Variations in immunotherapy effectiveness according to risk assessments. **C** – Proportion of various immunotherapy reactions categorized by risk group

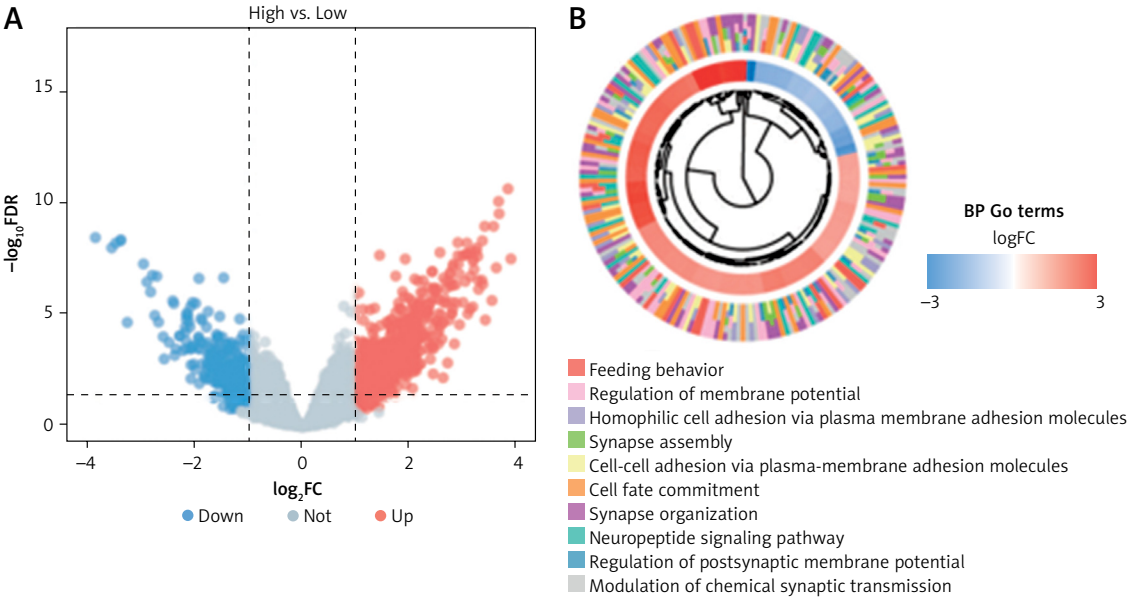
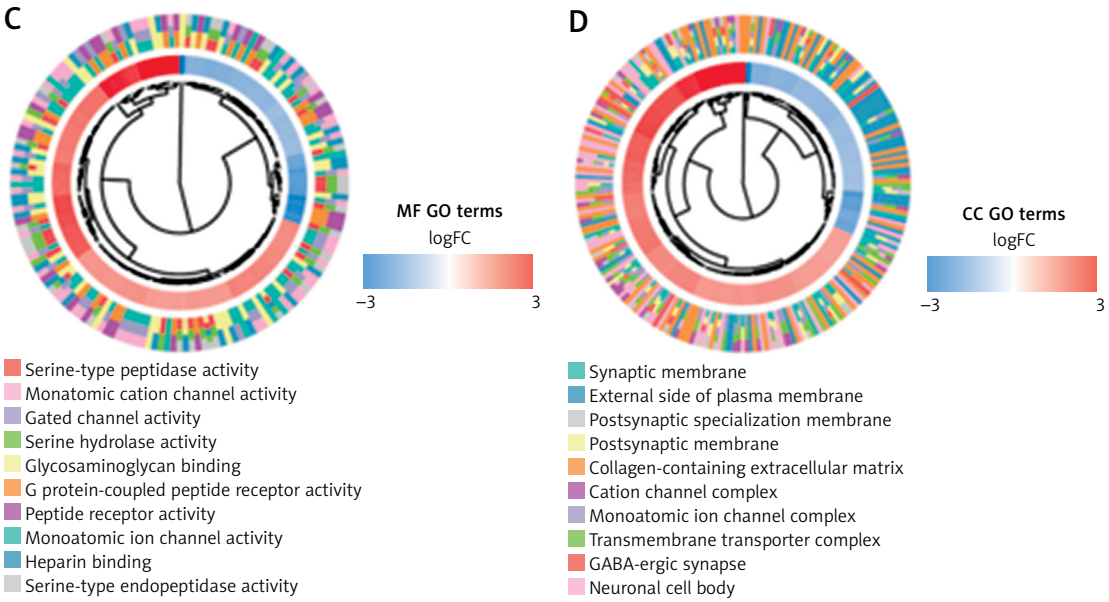
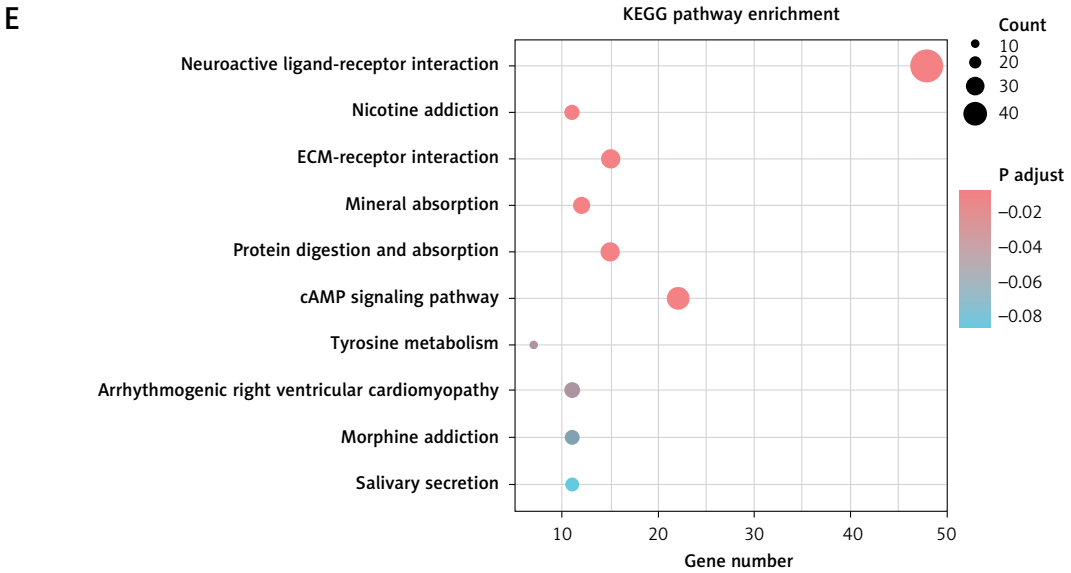


Figure 8. Investigation of biological roles and pathway activities in high- and low-risk groups. **A** – Volcano map illustrating genes expressed differently between high- and low-risk groups. Functional analysis in (**B**) Biological Activities (BP)





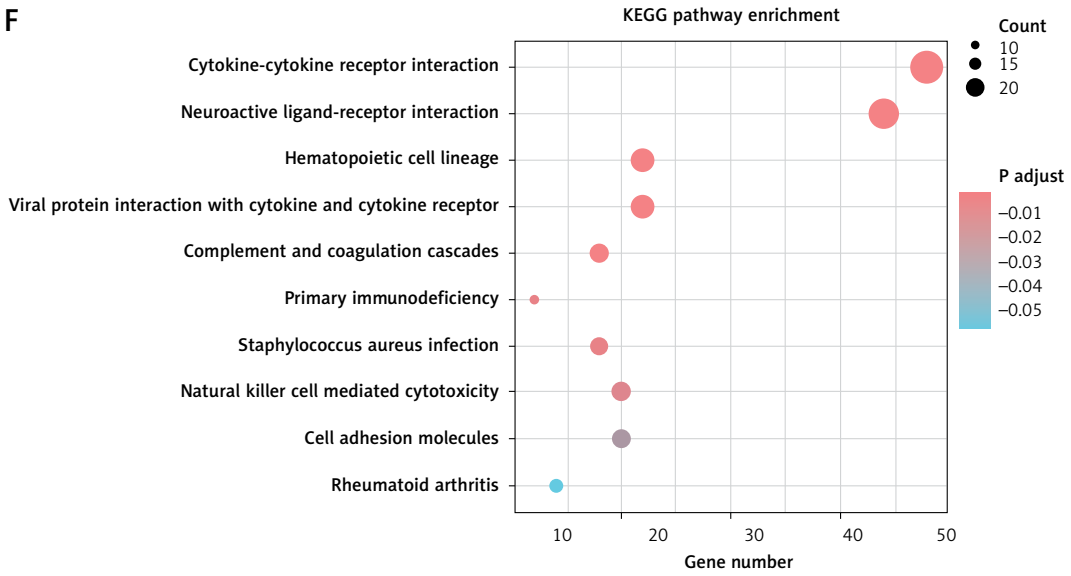


Figure 8. Cont. Functional analysis in (**C**) Molecular Roles (MF), and (**D**) Cellular Structures (CC). **E** – KEGG enrichment assessment of increased gene expression. **F** – KEGG enrichment assessment of downregulated genes

cess (BP) category (Figure 8 B), protein metabolism pathways within the Molecular Function (MF) category (Figure 8 C), and neuroregulation-related pathways within the Cellular Component (CC) category (Figure 8 D). Additionally, KEGG analysis indicated that upregulated genes were enriched in neuroregulation and protein metabolism pathways (Figure 8 E), whereas downregulated genes were associated with immune regulation-related pathways (Figure 8 F).

Analysis of the relationship between TME and risk score-related cell types based on single-cell sequencing

To investigate the relationship between the TME and cell types associated with risk scores, we analyzed single-cell sequencing data from 11 OSA patients in the GSE152048 dataset. After quality control and batch effect removal, we clustered and annotated the filtered cells into nine major cell types: macrophages, chondroblastic cells, osteoclasts, T cells, cycling cells, monocytes, osteoblastic cells, pericytes, endothelial cells, NK cells, and mast cells (Figure 9 A). Using the SCISSOR algorithm alongside sequencing data from TARGET-OS patients and risk group information, we identified cell types correlated with different risk levels (Figure 9 B) [25]. Consistent with expectations, we observed more high-risk-associated cell types in patients with recurrence and metastasis (Figure 9 C).

We then employed CellChat to infer overall intercellular communication based on ligand-receptor signaling. As illustrated in Figure 9 D, the results depict the number of cells involved in in-

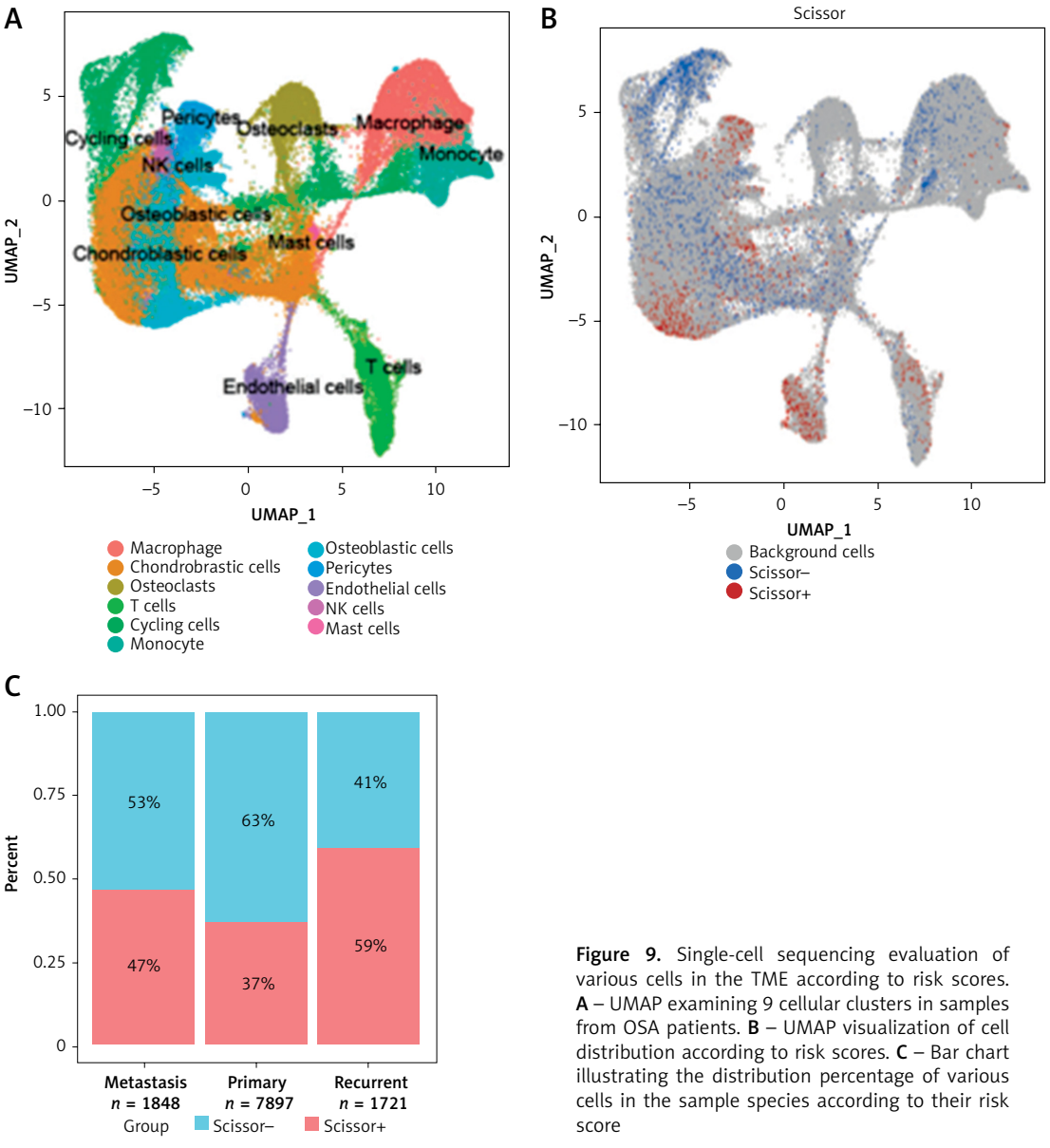


Figure 9. Single-cell sequencing evaluation of various cells in the TME according to risk scores. **A** – UMAP examining 9 cellular clusters in samples from OSA patients. **B** – UMAP visualization of cell distribution according to risk scores. **C** – Bar chart illustrating the distribution percentage of various cells in the sample species according to their risk score

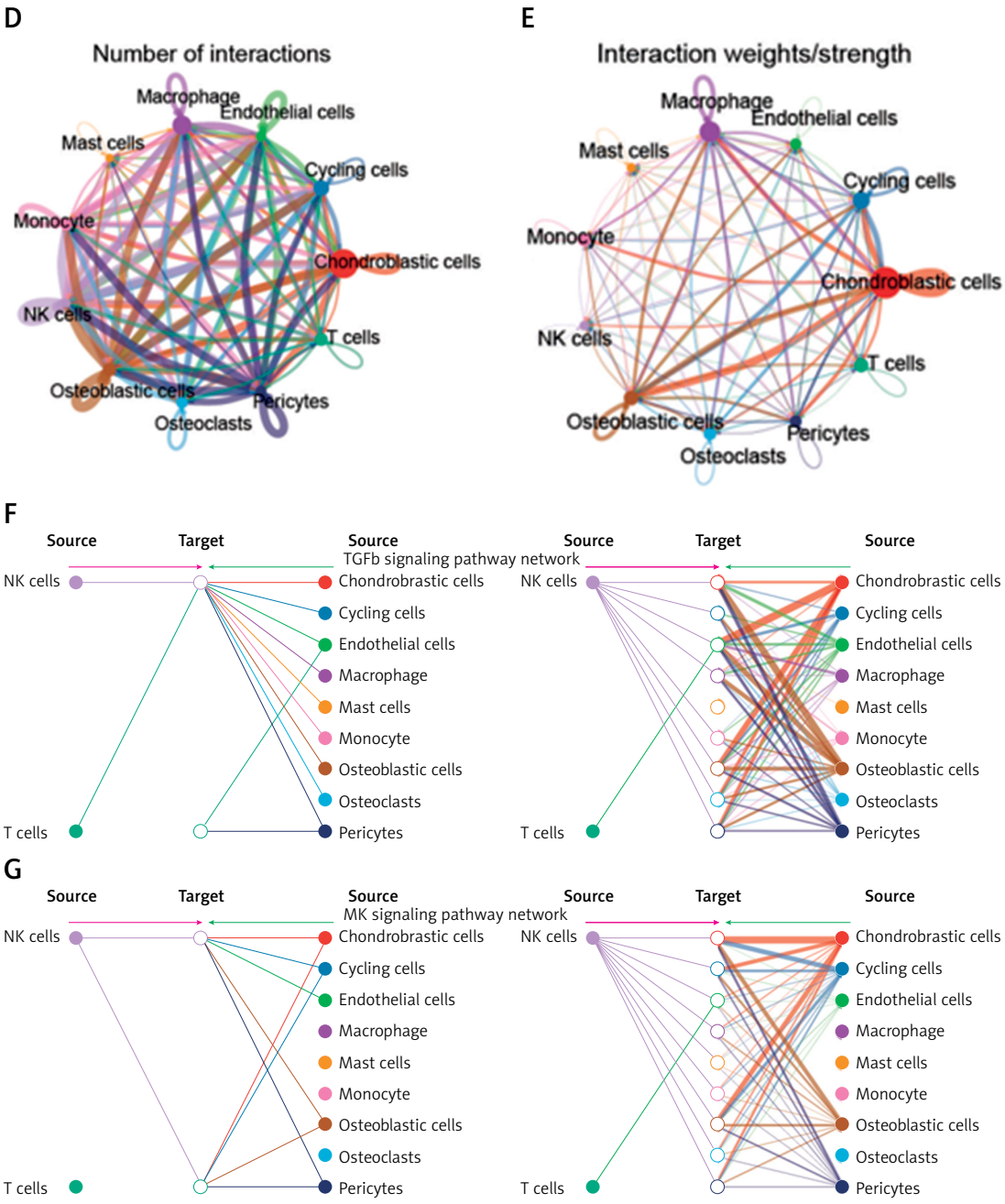


Figure 9. Cont. **D** – The number of cells engaged in communication and interaction with one another is depicted. Different colored circles represent the cell count, with larger circles signifying a higher number of cells involved. **E** – Intensity of intercellular communication exchanges: the thicker the line, the greater the intensity. Examination of cell interactions in the TGFb (**F**) and MKK signaling pathway (**G**)

teractions, while Figure 9 E shows the frequency of interactions among different cell types. Collectively, these findings indicate significant cell-cell communication, which is essential for understanding immune cell functions within the TME. Furthermore, transforming growth factor β (TGFb, Figure 9 F) and mitogen-activated protein kinase kinase kinase (MKK, Figure 9 G) signaling pathways were identified as potentially involved in cell proliferation, differentiation, and immune regulation, possibly playing multifaceted roles in tumor progression. We further analyzed the relationships between the identified cell types and these pathways, and found distinct intercellular communication patterns targeting these pathways. Additionally, we assessed the distribution of characteristic genes across immune cell types and observed that MYC and SCD1 had superior cell-type-specific expression compared to other genes (Supplementary Figure S2).

Comprehensive analysis of potential anti-OSA drugs

This study employed the CellMiner database to predict the correlation between feature genes and drug sensitivity, identifying a significant positive relationship between MYC and DMAPT (Figure 10 A), obatoclax (Figure 10 B), 8-chloro-adenosine (Figure 10 C), and palbociclib (Figure 10 D). We also conducted a statistical analysis of approved drugs targeting feature genes, providing theoretical support for selecting suitable therapeutic agents for OSA patients (Figure 10 E). Notably, our analysis of drug sensitivity between risk groups showed that patients in the low-risk group had significantly lower IC_{50} values for cisplatin (Figure 10 F) and temozolomide

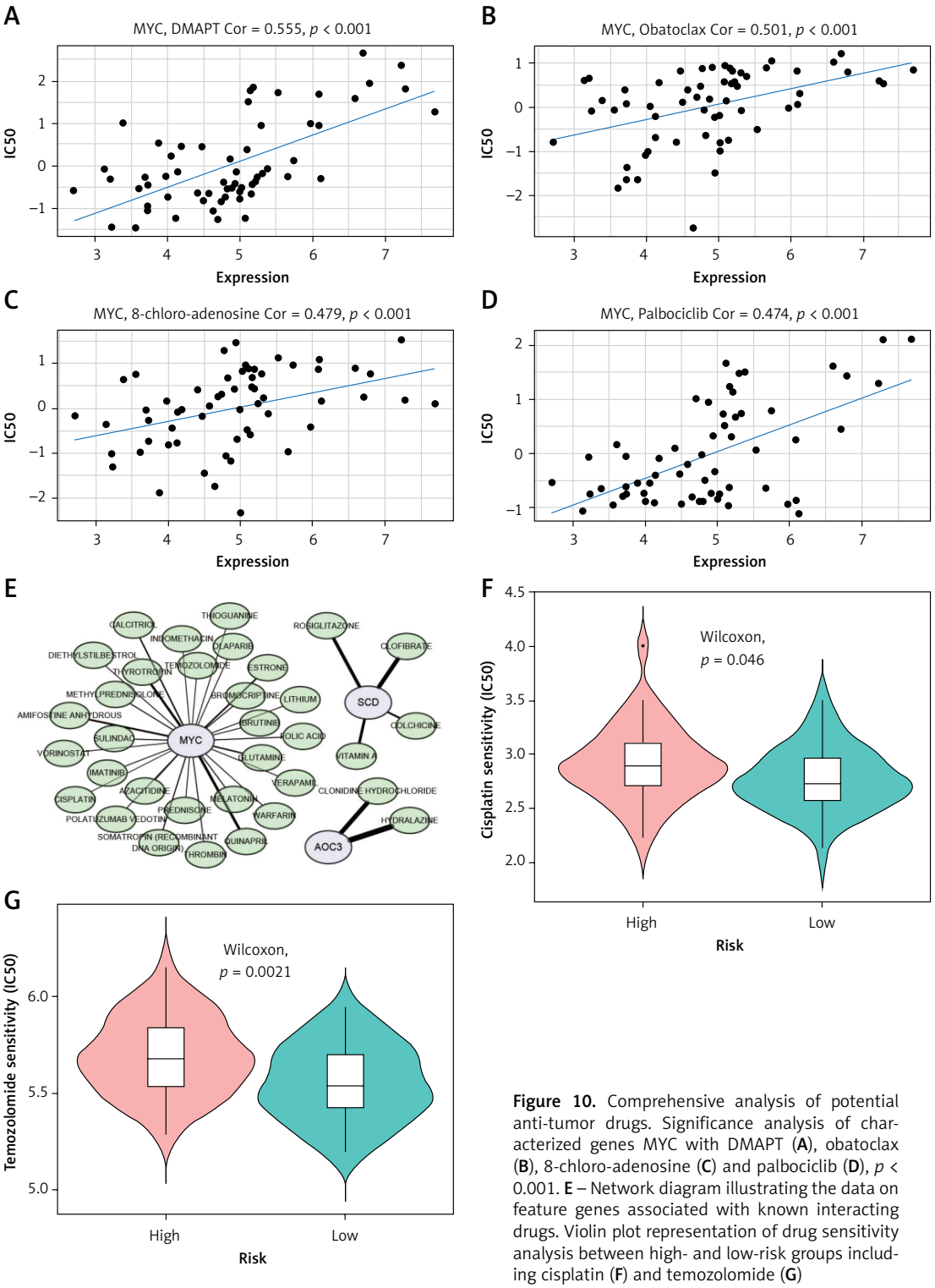


Figure 10. Comprehensive analysis of potential anti-tumor drugs. Significance analysis of characterized genes MYC with DMAPT (**A**), obatoclax (**B**), 8-chloro-adenosine (**C**) and palbociclib (**D**), $p < 0.001$. **E** – Network diagram illustrating the data on feature genes associated with known interacting drugs. Violin plot representation of drug sensitivity analysis between high- and low-risk groups including cisplatin (**F**) and temozolomide (**G**)

(Figure 10 G), indicating that these drugs may be more effective in low-risk patients.

Comprehensive experimental analysis of characteristic gene expression, cell apoptosis, and cytotoxicity

Next, we validated the expression levels of the characteristic genes in the osteoblastic cell line hFOB1.19 and the OSA cell line U2OS. The qRT-PCR results (Figure 11 A) showed that EPYC was significantly overexpressed in U2OS cells. Similarly, SCD1 and AOC3 were also significantly upregulated in OSA cells. In contrast, no significant differences were observed in the expression of MYC and KLK2. These findings further confirm the differential expression of characteristic genes between normal and OSA cells. The MTT cytotoxicity assay results (Figure 11 B) demonstrated that both temozolomide and cisplatin exhibited concentration-dependent enhanced inhibitory effects on the proliferation of OSA cell lines U2OS and SAOS2. SAOS2 cells showed higher sensitivity to both drugs, with a significantly lower IC_{50} (81.52 μM) for temozolomide compared to U2OS cells (112.4 μM), and a markedly lower IC_{50} (4.087 μM) for cisplatin (9.314 μM). TUNEL apoptosis assays further corroborated the heightened sensitivity of SAOS2 cells, revealing a significantly higher proportion of TUNEL positive cells in SAOS2 cells following treatment with either temozolomide or cisplatin, compared to U2OS cells (Figures 11 C, D). Collectively, these data consistently demonstrate that SAOS2 cells possess higher sensitivity than U2OS cells to temozolomide- and cisplatin-induced cytotoxicity and apoptosis.

Discussion

Immunotherapy plays a crucial role in tumor treatment. Although it has not yet been approved for OSA, several approaches – including immune checkpoint inhibitors, bispecific antibodies, and chimeric antigen receptor (CAR) T cells – are actively undergoing clinical development [26]. Consequently, research on immunotherapy for OSA is expected to become a key focus in the field. CMRGs are essential for regulating T cell activity, maintaining immune balance, and modulating immune responses [27, 28]. This study evaluated the

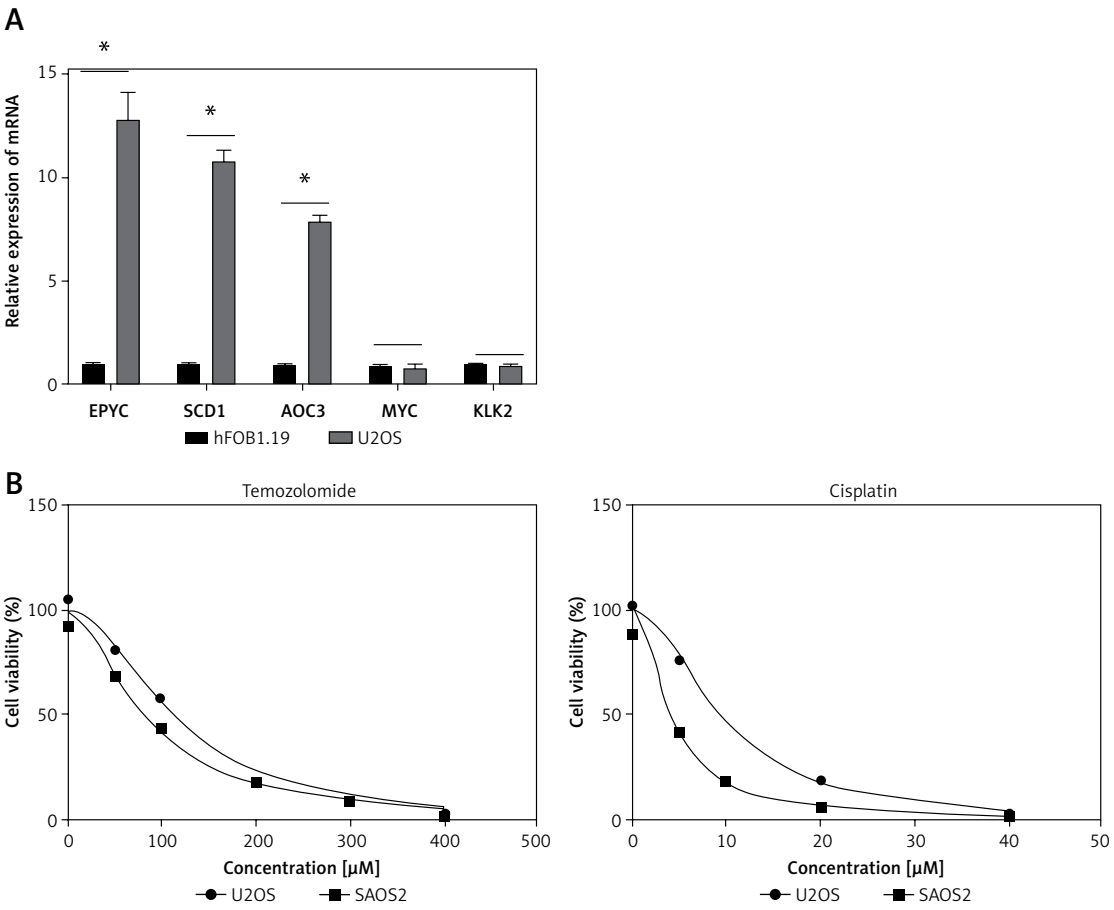


Figure 11. Comprehensive experimental analysis of characteristic gene expression, cell apoptosis, and cytotoxicity. **A** – qRT-PCR Results of EPYC, SCD1, and AOC3 in normal cells and OSA cells. **B** – MTT assay to detect the viability of U2OS and SAOS2 cells treated with different concentrations of temozolomide or cisplatin for 48 h. ns denotes no significant difference, * signifies $p < 0.05$

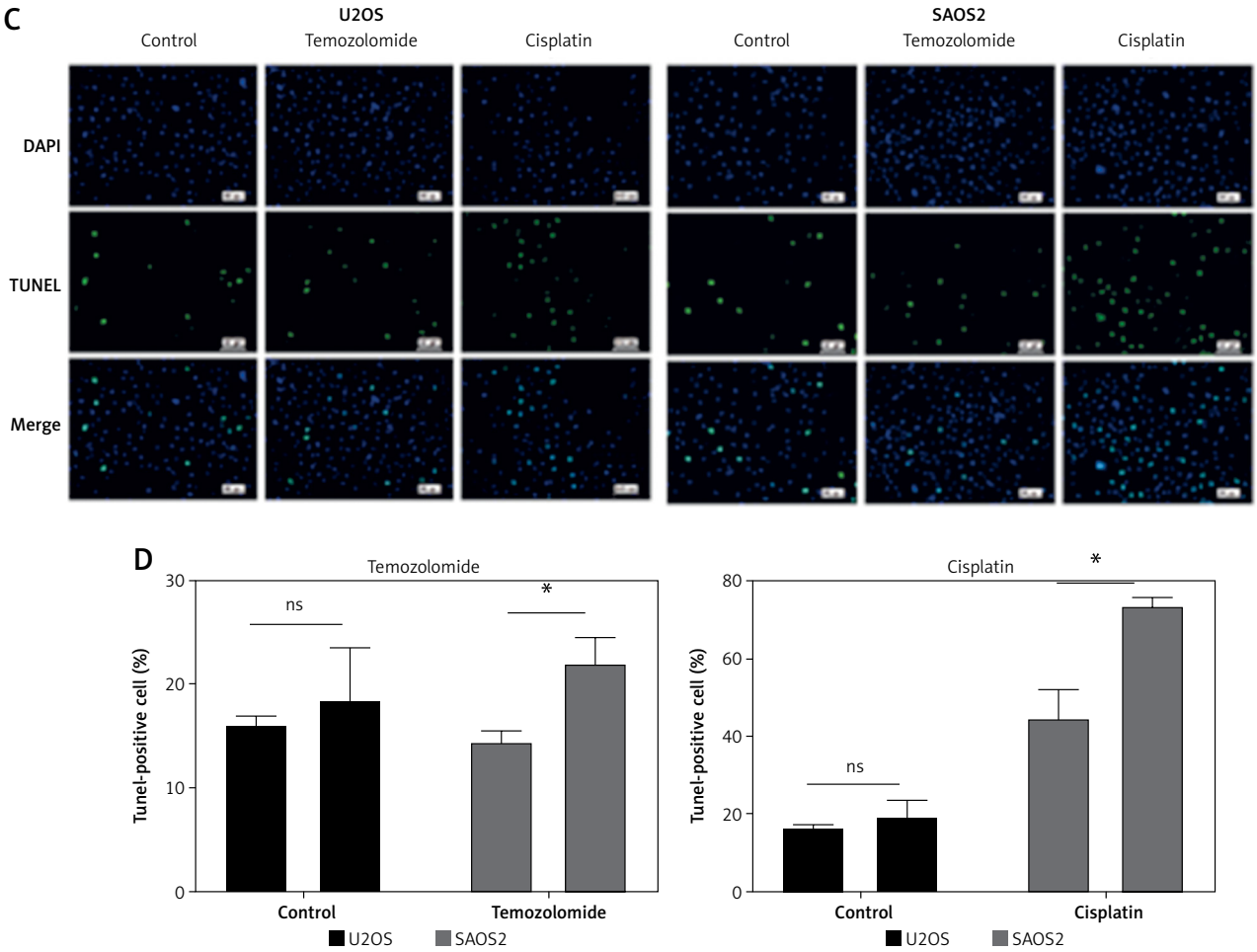


Figure 11. Cont. **C** – Representative images of TUNEL assay for cell apoptosis. **D** – Quantitative analysis results of TUNEL assay for cell apoptosis. ns denotes no significant difference, * signifies $p < 0.05$

prognostic outcomes of OSA patients based on CMRGs, and identified five characteristic genes: EPYC, SCD1, AOC3, MYC, and KLK2.

Epiphycan (EPYC), located on human chromosome 12, is a protein-coding gene composed of seven exons [29]. Its primary function is to regulate fibril formation through interactions with collagen fibrils and other extracellular matrix proteins [30]. EPYC has been implicated in various diseases. Liang *et al.* demonstrated that EPYC serves as a diagnostic marker for osteoarthritis, supported by both machine learning and *in vitro* experiments [31]. Similarly, Zhang *et al.* confirmed EPYC as a characteristic gene for osteoarthritis and reported a significant correlation between EPYC expression and immune infiltration [32]. In addition, EPYC has been identified as a prognostic biomarker for pancreatic cancer [30]. Our results revealed that EPYC is highly expressed in OSA tissues, and that patients in the low-risk group exhibited significantly better survival outcomes. Furthermore, EPYC expression was positively correlated with immune cell infiltration, suggesting its potential as a prognostic biomarker for OSA.

Stearoyl-CoA desaturase 1 (SCD1) is an enzyme located in the endoplasmic reticulum, which catalyzes the desaturation of saturated fatty acids (SFAs) [33]. A review study reported that SCD1 acts as an autophagy inducer, affecting cancer cell proliferation and metastasis [34]. In colorectal cancer, SCD1 plays a key role in drug-induced growth inhibition, and SCD1 knockout enhances sensitivity to ferroptosis [35]. Notably, Cai *et al.* found that SCD1 regulates the Akt/mTOR pathway, promoting lipid metabolism and enhancing OSA cell proliferation [36].

Amine oxidase copper containing 3 (AOC3) encodes a cell adhesion protein that is involved in lymphocyte extravasation and recirculation [37]. Dysregulation of AOC3 expression has been shown to influence cancer progression. Studies report that AOC3 expression is decreased in colorectal cancer tissues and serum, with low levels correlating with poor prognosis [38, 39]. Conversely, high AOC3 expression in thymic carcinoma has

been significantly associated with unfavorable prognosis [40].

MYC is a transcription factor and a key driver of human tumorigenesis. The MYC protein mainly regulates transcriptional processes, including elongation, DNA replication, and cell cycle progression [41, 42]. Targeting MYC has emerged as a potential strategy for cancer therapy [43, 44].

Human kallikrein 2 (KLK2) belongs to the kallikrein gene family and functions as a serine protease [45, 46]. Recent studies suggest that KLK2 may be a therapeutic target in prostate cancer, where elevated KLK2 expression correlates with increased proliferation and reduced apoptosis [47]. KLK2 has also been established as a prognostic biomarker for prostate cancer [48]. Our study explored KLK2 as a component of a prognostic model for OSA, demonstrating its potential value in predicting survival.

In conclusion, this study identifies five characteristic genes based on CMRGs to construct a prognostic model, which may support personalized treatment strategies for OSA patients and inform clinical decision-making.

Most immunotherapy strategies rely on the patient's intrinsic immune response, typically progressing through three stages: immune surveillance, self-regulation, and immune evasion [14]. Immune checkpoint inhibitors are central to these mechanisms and have shown promise in treating OSA [14, 49]. CTLA-4 binds to B7 on Tregs and antigen-presenting cells, thereby suppressing T cell activity. Blocking this interaction can restore T cell functionality [49]. Notably, anti-PD-1 therapy in an OSA mouse model led to increased expression of GZMB in T cells [50, 51]. Yoshida *et al*. reported a positive correlation between GZMB and IFN-γ expression, with elevated GZMB levels linked to improved survival in OSA patients [52]. These findings highlight the potential relevance of GZMB in immunotherapy efficacy. Our analysis revealed elevated GZMB expression in the low-risk group, along with other immune checkpoint-related genes such as BTK, BTLA, CD40, CD44, LAG3, LAIR1, TNFRSF9, and TNFSF15, suggesting that low-risk patients may have greater potential to respond to immunotherapy.

Dimethylaminoparthenolide (DMAPT) is an anti-inflammatory compound that has been reported to inhibit prostate cancer [53] and bladder cancer progression [54]. Obatoclax, a BCL2 family inhibitor, induces thyroid cancer cell death by disrupting lysosomal function [55]. 8-chloro-adenosine is a nucleoside analog that has been investigated in leukemia research [56]. Palbociclib is an orally available CDK4/6 inhibitor, which suppresses proliferation and induces cell cycle arrest, with broad application in breast cancer therapy [57, 58]. Our study identified a significant positive correlation between MYC expression and the IC_{50} values of these drugs. Moreover, our analysis revealed that low-risk patients showed greater predicted sensitivity to cisplatin and temozolomide, supporting their potential clinical utility in this subgroup.

Our correlation analysis (Supplementary Figure S1) revealed associations between the CMRG-based signature and classic oncogenes. The negative correlation between KLK2 and FAS may indicate an association between KLK2 expression and FAS-mediated apoptosis, a mechanism known to contribute to chemotherapy resistance [59]. Conversely, the positive correlation between SCD1 and NRAS is consistent with NRAS's role in activating SREBP-1c-driven lipogenesis – a pathway that increases the production of monounsaturated fatty acids (MUFA) through SCD1-mediated desaturation, thereby potentially enhancing membrane fluidity, oncogenic signaling, and tumor cell proliferation [60, 61]. Notably, the absence of correlation with TP53 – a gene frequently mutated in OSA – may indicate that our CMRG signature reflects biological pathways distinct from canonical tumor suppressor mechanisms.

To our knowledge, this is the first comprehensive study to construct a CMRG-based prognostic model for OSA that integrates subtype classification, immune profiling, drug sensitivity prediction, and experimental validation, thereby expanding the understanding of immune regulation in OSA and proposing novel clinical biomarkers. However, several limitations warrant consideration: the analyses primarily rely on public databases, which may introduce population bias; although qRT-PCR validated gene expression, further *in vivo* and clinical studies are needed to confirm the functional roles of these genes; and the risk model's generalizability requires external validation due to the lack of prospective cohorts.

In conclusion, this study subdivided OSA samples into three subtypes based on CMRGs and analyzed the differences in immune cell infiltration levels among the subtypes, revealing that subtype 3 exhibited significantly higher immune infiltration levels than subtypes 1 and 2. By merging subtypes 2 and 3, we identified differentially expressed genes, ultimately selecting five characteristic genes through LASSO and multivariable regression analysis to construct a prognostic model for OSA. Our results showed that the low-risk group had better prognostic outcomes, suggesting that patients in this group may have greater potential to respond to immunotherapy. Additionally, single-cell sequencing results characterized the distribution of immune cells and the expression levels of characteristic genes within these cells. In summary, the prognostic prediction model devel-

oped in this study may help inform strategies to enhance survival rates in OSA patients, providing a theoretical basis for personalized treatment approaches.

Acknowledgments

Sen Cai and Lingtao Xu are co-first authors.

Funding

No external funding.

Ethical approval

Not applicable.

Conflict of interest

The authors declare no conflict of interest.

References

1. Arndt CA, Rose PS, Folpe AL, et al. Common musculoskeletal tumors of childhood and adolescence. Mayo Clin Proc 2012; 87: 475-87.
2. Huang X, Zhao J, Bai J, et al. Risk and clinicopathological features of osteosarcoma metastasis to the lung: a population-based study. J Bone Oncol 2019; 16: 100230.
3. Eaton BR, Schwarz R, Vatner R, et al. Osteosarcoma. Pediatr Blood Cancer 2021; 68 Suppl 2: e28352.
4. Gianferante DM, Mirabello L, Savage SA. Germline and somatic genetics of osteosarcoma – connecting aetiology, biology and therapy. Nat Rev Endocrinol 2017; 13: 480-91.
5. Li J, Tang X, Du Y, et al. Establishment of an autophagy-related clinical prognosis model for predicting the overall survival of osteosarcoma. Biomed Res Int 2021; 2021: 5428425.
6. Meltzer PS, Helman LJ. New horizons in the treatment of osteosarcoma. N Engl J Med 2021; 385: 2066-76.
7. Jamal-Hanjani M, Quezada SA, Larkin J, et al. Translational implications of tumor heterogeneity. Clin Cancer Res 2015; 21: 1258-66.
8. Wu C, Gong S, Duan Y, et al. A tumor microenvironment-based prognostic index for osteosarcoma. J Biomed Sci 2023; 30: 23.
9. Momen M, Kohler NL, Binversie EE, et al. Heritability and genetic variance estimation of osteosarcoma (OSA) in Irish Wolfhound, using deep pedigree information. Canine Med Genet 2021; 8: 9.
10. Wei X, Feng J, Chen L, et al. METTL3-mediated m6A modification of LINC00520 confers glycolysis and chemoresistance in osteosarcoma via suppressing ubiquitination of ENO1. Cancer Lett 2024; 611: 217194.
11. Jiang M, Jike Y, Liu K, et al. Exosome-mediated miR-144-3p promotes ferroptosis to inhibit osteosarcoma proliferation, migration, and invasion through regulating ZEB1. Mol Cancer 2023; 22: 113.
12. Cheng X, Bian C, Zhang Y, Gu H, Chen G, Wu L. APOE suppresses osteosarcoma by modulating ferroptosis through the mTOR/Stat3 signaling pathway. Arch Med Sci 2025; 21: 2647-70.
13. Bilotta MT, Antignani A, Fitzgerald DJ. Managing the TME to improve the efficacy of cancer therapy. Front Immunol 2022; 13: 954992.
14. Chen C, Xie L, Ren T, et al. Immunotherapy for osteosarcoma: fundamental mechanism, rationale, and recent breakthroughs. Cancer Lett 2021; 500: 1-10.
15. Singh S, Hassan D, Aldawsari HM, et al. Immune checkpoint inhibitors: a promising anticancer therapy. Drug Discov Today 2020; 25: 223-9.
16. Sanmamed MF, Chen L. A paradigm shift in cancer immunotherapy: from enhancement to normalization. Cell 2018; 175: 313-26.
17. Capece D, Verzella D, Fischietti M, et al. Targeting costimulatory molecules to improve antitumor immunity. J Biomed Biotechnol 2012; 2012: 926321.
18. Fan MK, Qi LL, Zhang Q, et al. The updated status and future direction of immunotherapy targeting B7-H1/PD-1 in osteosarcoma. Cancer Manag Res 2021; 13: 757-64.
19. Zhang C, Zhang Z, Li F, et al. Large-scale analysis reveals the specific clinical and immune features of B7-H3 in glioma. Oncoimmunology 2018; 7: e1461304.
20. Janakiram M, Chinai JM, Zhao A, et al. HHLA2 and TMIGD2: new immunotherapeutic targets of the B7 and CD28 families. Oncoimmunology 2015; 4: e1026534.
21. Ward-Kavanagh LK, Lin WW, Šedý JR, et al. The TNF receptor superfamily in co-stimulating and co-inhibitory responses. Immunity 2016; 44: 1005-19.
22. Zhang C, Zhang Z, Sun N, et al. Identification of a co-stimulatory molecule-based signature for predicting prognosis risk and immunotherapy response in patients with lung adenocarcinoma. Oncoimmunology 2020; 9: 1824641.
23. Li H, Liu S, Li C, et al. TNF family-based signature predicts prognosis, tumor microenvironment, and molecular subtypes in bladder carcinoma. Front Cell Dev Biol 2021; 9: 800967.
24. Ren Q, Zhang P, Lin H, et al. A novel signature predicts prognosis and immunotherapy in lung adenocarcinoma based on cancer-associated fibroblasts. Front Immunol 2023; 14: 1201573.
25. Sun D, Guan X, Moran AE, et al. Identifying phenotype-associated subpopulations by integrating bulk and single-cell sequencing data. Nat Biotechnol 2022; 40: 527-38.
26. Yu S, Yao X. Advances on immunotherapy for osteosarcoma. Mol Cancer 2024; 23: 192.
27. Bäck M, Weber C, Lutgens E. Regulation of atherosclerotic plaque inflammation. J Intern Med 2015; 278: 462-82.
28. Zhao Y, Zheng Q, Jin L. The role of B7 family molecules in maternal-fetal immunity. Front Immunol 2020; 11: 458.
29. Hanada Y, Nakamura Y, Ishida Y, et al. Epiphycan is specifically expressed in cochlear supporting cells and is necessary for normal hearing. Biochem Biophys Res Commun 2017; 492: 379-85.
30. Yang Z, Li H, Hao J, et al. EPYC functions as a novel prognostic biomarker for pancreatic cancer. Sci Rep 2024; 14: 719.
31. Liang Y, Lin F, Huang Y. Identification of biomarkers associated with diagnosis of osteoarthritis patients based on bioinformatics and machine learning. J Immunol Res 2022; 2022: 5600190.
32. Zhang J, Zhang S, Zhou Y, et al. KLF9 and EPYC acting as feature genes for osteoarthritis and their association with immune infiltration. J Orthop Surg Res 2022; 17: 365.
33. Paton CM, Ntambi JM. Biochemical and physiological function of stearoyl-CoA desaturase. Am J Physiol Endocrinol Metab 2009; 297: E28-37.
34. Ascenzi F, De Vitis C, Maugeri-Saccà M, et al. SCD1, autophagy and cancer: implications for therapy. J Exp Clin Cancer Res 2021; 40: 265.

35. Chen H, Qi Q, Wu N, et al. Aspirin promotes RSL3-induced ferroptosis by suppressing mTOR/SREBP-1/SCD1-mediated lipogenesis in PIK3CA-mutant colorectal cancer. Redox Biol 2022; 55: 102426.
36. Cai F, Liu L, Bo Y, et al. LncRNA RPARP-AS1 promotes the progression of osteosarcoma cells through regulating lipid metabolism. BMC Cancer 2024; 24: 166.
37. Boyer DS, Rippmann JF, Ehrlich MS, et al. Amine oxidase copper-containing 3 (AOC3) inhibition: a potential novel target for the management of diabetic retinopathy. Int J Retina Vitreous 2021; 7: 30.
38. Ahmad Zawawi SS, Mohd Azram NAS, Sulong S, et al. Identification of AOC3 and LRRC17 as colonic fibroblast activation markers and their potential roles in colorectal cancer progression. Asian Pac J Cancer Prev 2023; 24: 3099-107.
39. Ward ST, Weston CJ, Shepherd EL, et al. Evaluation of serum and tissue levels of VAP-1 in colorectal cancer. BMC Cancer 2016; 16: 154.
40. Lai YC, Chang SJ, Kostoro J, et al. Vascular adhesion protein-1 as indicator of breast cancer tumor aggressiveness and invasiveness. Apmis 2018; 126: 755-61.
41. Lourenco C, Resetca D, Redel C, et al. MYC protein interactors in gene transcription and cancer. Nat Rev Cancer 2021; 21: 579-91.
42. Baluapuri A, Wolf E, Eilers M. Target gene-independent functions of MYC oncoproteins. Nat Rev Mol Cell Biol 2020; 21: 255-67.
43. Duffy MJ, O'Grady S, Tang M, et al. MYC as a target for cancer treatment. Cancer Treat Rev 2021; 94: 102154.
44. Chen H, Liu H, Qing G. Targeting oncogenic Myc as a strategy for cancer treatment. Signal Transduct Target Ther 2018; 3: 5.
45. Avgeris M, Mavridis K, Scorilas A. Kallikrein-related peptidase genes as promising biomarkers for prognosis and monitoring of human malignancies. Biol Chem 2010; 391: 505-11.
46. Paniagua-Herranz L, Moreno I, Nieto-Jiménez C, et al. Genomic and immunologic correlates in prostate cancer with high expression of KLK2. Int J Mol Sci 2024; 25: 2222.
47. Shang Z, Niu Y, Cai Q, et al. Human kallikrein 2 (KLK2) promotes prostate cancer cell growth via function as a modulator to promote the ARA70-enhanced androgen receptor transactivation. Tumour Biol 2014; 35: 1881-90.
48. Kohli M, Rothberg PG, Feng C, et al. Exploratory study of a KLK2 polymorphism as a prognostic marker in prostate cancer. Cancer Biomark 2010; 7: 101-8.
49. Zhang Z, Tan X, Jiang Z, et al. Immune checkpoint inhibitors in osteosarcoma: a hopeful and challenging future. Front Pharmacol 2022; 13: 1031527.
50. Zheng B, Ren T, Huang Y, et al. PD-1 axis expression in musculoskeletal tumors and antitumor effect of nivolumab in osteosarcoma model of humanized mouse. J Hematol Oncol 2018; 11: 16.
51. Ratti C, Botti L, Cancila V, et al. Trabectedin overrides osteosarcoma differentiative block and reprograms the tumor immune environment enabling effective combination with immune checkpoint inhibitors. Clin Cancer Res 2017; 23: 5149-61.
52. Yoshida K, Okamoto M, Sasaki J, et al. Clinical outcome of osteosarcoma and its correlation with programmed death-ligand 1 and T cell activation markers. Onco Targets Ther 2019; 12: 2513-8.
53. Mendonca MS, Turchan WT, Alpuche ME, et al. DMAPT inhibits NF-κB activity and increases sensitivity of prostate cancer cells to X-rays in vitro and in tumor xenografts in vivo. Free Radic Biol Med 2017; 112: 318-26.
54. Gil da Costa RM, Levesque C, Bianchi-Frias D, et al. Pharmacological NF-κB inhibition decreases cisplatin chemoresistance in muscle-invasive bladder cancer and reduces cisplatin-induced toxicities. Mol Oncol 2023; 17: 2709-27.
55. Champa D, Orlacchio A, Patel B, et al. Obatoclax kills anaplastic thyroid cancer cells by inducing lysosome neutralization and necrosis. Oncotarget 2016; 7: 34453-71.
56. Buettner R, Nguyen LXT, Morales C, et al. Targeting the metabolic vulnerability of acute myeloid leukemia blasts with a combination of venetoclax and 8-chloro-adenosine. J Hematol Oncol 2021; 14: 70.
57. Rugo HS, Finn RS, Diéras V, et al. Palbociclib plus letrozole as first-line therapy in estrogen receptor-positive/human epidermal growth factor receptor 2-negative advanced breast cancer with extended follow-up. Breast Cancer Res Treat 2019; 174: 719-29.
58. Braal CL, Jongbloed EM, Wilting SM, et al. Inhibiting CDK4/6 in breast cancer with palbociclib, ribociclib, and abemaciclib: similarities and differences. Drugs 2021; 81: 317-31.
59. Zhao T, Li W, Chen J, et al. Genomic variants in Fas-mediated apoptosis pathway predict a poor response to platinum-based chemotherapy for chinese gastric cancer patients. J Cancer 2021; 12: 849-59.
60. Zhao Q, Lin X, Wang G. Targeting SREBP-1-mediated lipogenesis as potential strategies for cancer. Front Oncol 2022; 12: 952371.
61. Tracz-Gaszewska Z, Dobrzyn P. Stearoyl-CoA desaturase 1 as a therapeutic target for the treatment of cancer. Cancers 2019; 11: 948.